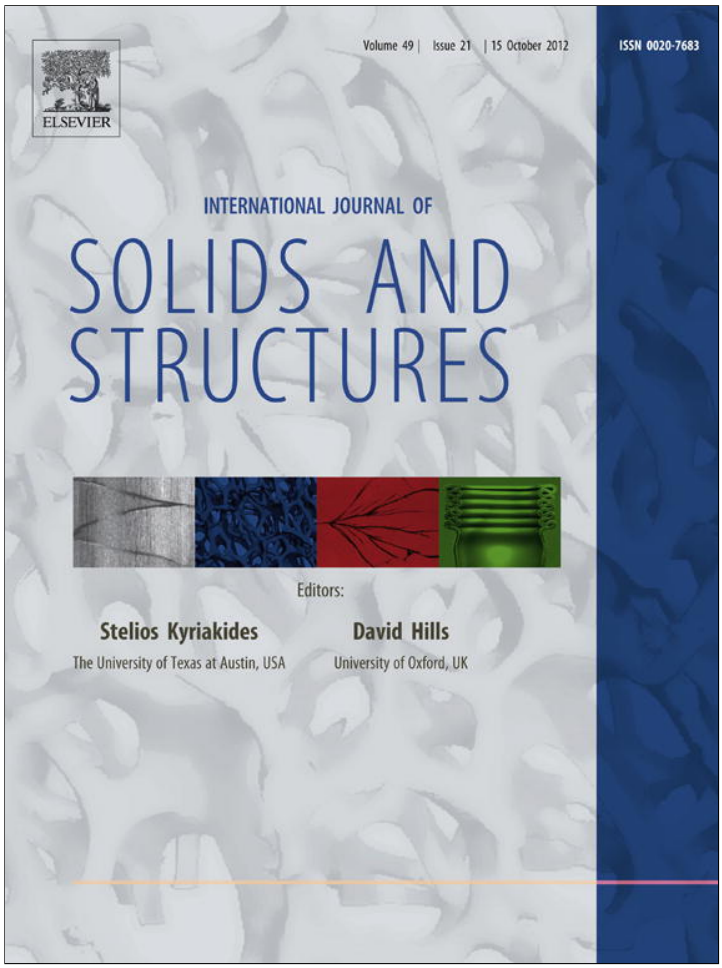

International Journal of Solids and Structures 49 (2012) 2990–3007

Contents lists available at SciVerse ScienceDirect

International Journal of Solids and Structures

journal homepage: www.elsevier.com/locate/ijsolstr

# A micromorphic model for steel fiber reinforced concrete

J. Oliver [a], D.F. Mora [a], A.E. Huespe [b,*], R. Weyler [c]

[a] E.T.S. Enginyers de Camins, Canals i Ports, Technical University of Catalonia (UPC), Campus Nord UPC (mòdul C-1), Jordi Girona 3, 08034 Bacelona, Spain
[b] CIMEC/CONICET-UNL, Güemes 3450, 3000 Santa Fe, Argentina
[c] E.T.S. Enginyeria Aeronáutica i Industrial, Technical University of Catalonia (UPC), Edifici TR45 (ETSEIAT), Terrassa, Spain

ARTICLE INFO

*Article history:*
Received 7 April 2012
Received in revised form 26 May 2012
Available online 12 June 2012

*Keywords:*
High performance fiber reinforced concrete (HPFRC)
Failure of HPFRC
Short reinforcement fibers
Micromorphic materials
Material multifield theory
Morphological descriptors

ABSTRACT

A new formulation to model the mechanical behavior of high performance fiber reinforced cement composites with arbitrarily oriented short fibers is presented.

The formulation can be considered as a two scale approach, in which the macroscopic model, at the structural level, takes into account the mesostructural phenomenon associated with the fiber–matrix interface bond/slip process. This phenomenon is contemplated by including, in the macroscopic description, a micromorphic field representing the relative fiber–cement displacement. Then, the theoretical framework, from which the governing equations of the problem are derived, can be assimilated to a specific case of the material multifield theory.

The balance equation derived for this model, connecting the micro stresses with the micromorphic forces, has a physical meaning related with the fiber–matrix bond slip mechanism. Differently to previous procedures in the literature, addressed to model fiber reinforced composites, where this equation has been added as an additional independent ingredient of the methodology, in the present approach it arises as a natural result derived from the multifield theory.

Every component of the composite is defined with a specific free energy and constitutive relation. The mixture theory is adopted to define the overall free energy of the composite, which is assumed to be homogeneously constituted, in the sense that every infinitesimal volume is occupied by all the components in a proportion given by the corresponding volume fraction.

The numerical model is assessed by means of a selected set of experiments that prove the viability of the present approach.



## 1. Introduction

Composite materials are the result of the combination of two or more components, and such that the properties of every one of them are clearly different from those of the composite. Generally, the composite material has better properties (with reference to overall strength, heat resistance, stiffness, etc.) than each one of the components. In particular, ceramic materials like cement, or concrete, are brittle in resisting tensile stresses, but the addition of discontinuous fibers leads to a dramatic improvement in their toughness during the fracture process. It is generally agreed that the fibers contribute primarily to the post-cracking response of the matrix, by providing resistance to the crack opening.

A classification proposed by Naaman (2007a) to determine if a fiber reinforced cement (FRC) composite qualifies as "high performance", is based on the shape of its average stress–elongation curve in the tensile test. For conventional FRC composite, this curve would show a response with softening behavior immediately after the cement cracking initiates. Alternatively, the qualification: "high performance", is used if this response shows a strain-hardening behavior after the initiation of cement cracking. Thus, high performance fiber reinforced cement composites, hereafter denoted HPFRC composite, exhibit a much higher ductility during the fracturing process than the conventional FRC composites. In this paper, we consider that the matrix of the HPFRC composite is constituted indistinctly of cement or concrete.

Experimental studies on HPFRC composites confirm that the mechanisms responsible for the macroscopic mechanical response mainly involve phenomena that occur at the mesostructural level. They are caused by the cement fracture and the ability of this component to transfer, during the fracture process, shearing stresses to the fibers through the interface bond. Consequently, the parameters governing the fiber–matrix bond response are a key aspect influencing significantly the macroscopic behavior (Guerrero and Naaman, 2000). From these considerations, an adequate mathematical model should contemplate this effect in order to capture the most salient mechanical features of the composite.

* Corresponding author.
*E-mail addresses:* xavier.oliver@upc.edu (J. Oliver), dfmoram@cimne.upc.edu (D.F. Mora), ahuespe@intec.unl.edu.ar (A.E. Huespe), rafael.weyler@upc.edu (R. Weyler).

0020-7683/$ - see front matter © 2012 Elsevier Ltd. All rights reserved.
http://dx.doi.org/10.1016/j.ijsolstr.2012.05.032

There exist several micromechanics-based models providing the effective elastic properties in composites, whose mechanical behavior is mostly governed by the fiber–matrix interaction at the mesostructural level: typically, the method of cells, the Mori–Tanaka method, Aveston–Cooper–Kelly theory (ACK theory), etc. The analysis in these methods is limited to a representative volume element (RVE) that includes one fiber and the surrounding matrix material. However, in spite of the useful predictive capabilities proven by these techniques, they still have limitations in analyzing composites with fibers randomly oriented.

A number of approaches to analyze HPFRC composites, take explicitly into account the above mentioned mesoscale phenomena, such as the models of Kabele (2007), Bolander and Sukumar (2005), Bolander et al. (2008), Pros et al. (2012), etc. Alternatively, other approaches simulate the mechanical response of this composites by means of phenomenological macroscopic models combined with fracture mechanics techniques, such as the models proposed by Boulfiza (1998), Ferrara Liberato (2000), Peng and Meyer (2000), Li and Li (2000), Zhang et al. (2002), Ferreira (2007), Sirijaroonchai et al. (2010), etc. We include in these types of approaches, the simplified model of Naaman (2007b).

In this paper, we describe a novel formulation based on the material multifield theory (Capriz, 1989; Mariano, 2002; Frémond and Nedjar, 1996) that also uses the classical mixture theory of Trusdell and Toupin (1960). The multifield theory is widely used in continuum mechanics; a number of applications were presented in the volume 38, issue 6–7 of this Journal, and mentioned in the Preface written by Capriz and Mariano (2001). Specifically, a large class of Multifield Theories covers the area of materials with microstructure, micromorphic materials, based on the addition of morphological descriptors.

The expression micromorphic material is used to denote those materials whose continuum behavior depends on the material micro-structure. Alternatively, they can be thought as macroscopic models endowed with properties coming from the structural interactions at lower length scales. This conceptual framework was introduced by Eringen (see Eringen and Suhubi, 1964) and Mindlin (1964) in the sixties, and provides a more general theoretical approach accounting for the microstrucural interactions, than that given by the classical internal variable approach. Subsequently, a considerable number of authors have followed this idea; see for example, the works of Forest (2009), Hirschberger et al. (2008), Marco (2006) and references cited therein.

Is within this type of theoretical context where we define the present HPFRC composite model. The main idea behind this formulation is to endow the macroscopic model with an internal morphology taking into account the fiber-matrix sliding mechanism, in such a way that the fiber can stretch independently of the matrix strain. The stretching along the fiber direction of both components, the cement and the fiber, are coupled by means of an interface having a specific constitutive response. As it is well known, the mixture theory alone cannot take into account this kind of mesostructural interactions among the components. Then, based on the multifield theory, we are able to add this feature into the model through the introduction of a new kinematical independent variable, the morphological descriptor that accounts for the mentioned fiber-matrix sliding mechanism. Then, the mechanical model of the composite can be described as a combination of three individual constitutive domains: the cement matrix, the fiber and the interface zone.

We emphasize at this point, that the main objective pursued in the present contribution is to describe the mathematical model of HPFRC composites in the context of a multifield theory. Then, those issues related with the numerical model implementation, as also, the detailed aspects about the fracture model approach here adopted, are only sketched in this work and they will be addressed in detail by the authors in a forthcoming paper.

An overview of the paper is as follows: Section 2 presents a brief description about the material multifield theory which is the background for the subsequent development of the HPFRC model. This model is presented in Section 3. Section 4 describes the problem governing equations connected with this composite material model. In Section 5, a short summary about the numerical implementation of the model, the finite element technology and the fracture model are only roughly outlined. The last Section of the paper provides the numerical assessment of the proposed formulation by means of the simulation of experimental tests published in the literature.

## 2. Brief description of a material multifield theory

A short summary of fundamental topics drawn from the so called multifield theory (Capriz, 1989; Mariano, 2002; Capriz and Mariano, 2001) is presented in this Section. The only objective that we pursue is to introduce the necessary ingredients providing the background for the posterior development of the HPFRC composite material model. Specific additional details of this theory can be found in the above mentioned works.

### 2.1. Configuration space

Les us consider a body $\mathfrak{B}$, with a reference placement $\mathfrak{B}_0$ in the three dimensional Euclidean space, undergoing a quasi-static loading process. The set of generalized external forces applied to the body are going to be precisely defined in the following section. The parameter $t$ represents a pseudo-time defining the sequence of increasing external loads during the interval of analysis: $[0,T]$.

The key idea of a material multifield theory is to assign to each material point $\mathbf{X}$ of $\mathfrak{B}_0$, the pair of kinematical variables $(\mathbf{x},\boldsymbol{\beta})$ that completely defines the configuration space of the body. The first element of the pair, $\mathbf{x}$, specifies the placement in the Euclidean space of the material particle $\mathbf{X}$ for all $t$, and the second one, $\boldsymbol{\beta}$, is a morphological descriptor collecting information about the mesostructure configuration, which is considered a kinematical descriptor being independent of $\mathbf{x}$. Both kinematical variables are sketched in Fig. 1 and defined by the maps:

$$\begin{aligned}&\mathbf{x}=\tilde{\mathbf{x}}(\mathbf{X},t)=\mathbf{X}+\mathbf{u}(\mathbf{X},t),\quad \forall\mathbf{X}\in\mathfrak{B}_0,\quad \forall t\in[0,T],\\&\boldsymbol{\beta}=\tilde{\boldsymbol{\beta}}(\mathbf{X},t),\quad \forall\mathbf{X}\in\mathfrak{B}_0,\quad \forall t\in[0,T].\end{aligned}\tag{1}$$

where $\mathbf{u}$ represents the displacement of the particle $\mathbf{X}$.

### 2.2. Balance equations

An additional and relevant aspect of the theory is to consider the possible mechanical interactions which are associated with the mesoscopic phenomenon characterized by the morphological descriptor $\boldsymbol{\beta}$. These interactions produce a mechanical power through the action of microforces $\boldsymbol{\zeta}$ acting on particles having the rate $\dot{\boldsymbol{\beta}}$, in a similar way as the conventional body forces $\mathbf{b}$ (per unit of volume) produce power through their action on particles with velocities $\dot{\mathbf{x}}$. Additionally to the power expended by the generalized forces $\mathbf{b}$ and $\boldsymbol{\zeta}$, it shall be considered those terms that produce power, such as the conventional surface tractions $\mathbf{t}^*=\boldsymbol{\sigma}\cdot\boldsymbol{\nu}$ acting on the boundary $\partial\mathfrak{B}_\sigma$ of $\mathfrak{B}$ and the mesostructural surface tractions: $\mathbf{S}\cdot\boldsymbol{\nu}$, caused by the microstresses $\mathbf{S}$, acting on the boundary $\partial\mathfrak{B}_\sigma$ of $\mathfrak{B}$. In both cases, the vector, $\boldsymbol{\nu}$, is the outward normal vector to the body boundary.

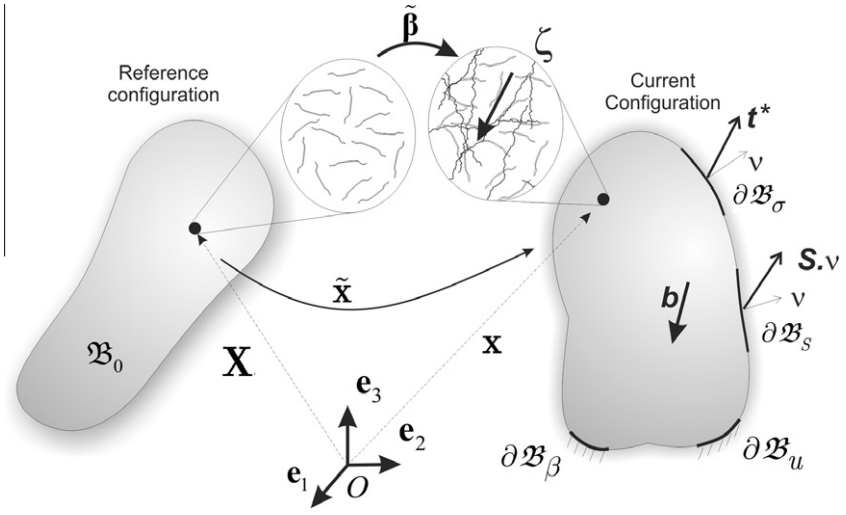


**Fig. 1.** Configuration space during the body motion defined in the context of a multifield theory including a morphological descriptor. Spatial placement is described by the map $\tilde{\mathbf{x}}$, while the micromorphic field $\boldsymbol{\beta}$ provides additional information about the material point mesostructural state. In this framework, the generalized forces are: $\mathbf{b}$, $\zeta$, $\mathbf{t}^*$ and $(\mathbf{S}\cdot\boldsymbol{\nu})$.

Introducing this concept into the mechanical model, the power expended by these generalized forces, and denoted as external power $P^{ext}$, is postulated as:

$$P^{ext} = \int_{\mathfrak{B}} (\mathbf{b}\cdot\dot{\mathbf{x}} + \zeta\cdot\dot{\boldsymbol{\beta}})d\Omega + \int_{\partial\mathfrak{B}_\sigma} \mathbf{t}^*\cdot\dot{\mathbf{x}}\,dA + \int_{\partial\mathfrak{B}_S} (\mathbf{S}\cdot\boldsymbol{\nu})\cdot\dot{\boldsymbol{\beta}}\,dA \tag{2}$$

The consequence of considering the interactions related with the morphological descriptors in (2), through $\zeta$ and $\mathbf{S}$, is that additional, non-conventional, balance equations arise in the model. They are derived from the external power $P^{ext}$ by considering the invariance of (2) under arbitrary observer changes, see Mariano (2002), and they are expressed as follows:

$$\nabla\cdot\boldsymbol{\sigma} + \mathbf{b} = \mathbf{0}; \quad \forall\mathbf{X}\in\mathfrak{B}_0 \tag{3}$$

$$\nabla\cdot\mathbf{S} - \mathbf{z} = \mathbf{0}; \quad \forall\mathbf{X}\in\mathfrak{B}_0 \tag{4}$$

In Eq. (3), $\boldsymbol{\sigma}$ is the conventional Cauchy stress tensor. Then, the local balance equation is the classical Cauchy equation, when inertial forces are neglected. Eq. (4) is the local balance of the substructural interactions, where, and without loss of generality, we have assumed that the external microforces are: $\zeta = \mathbf{0}$. A new object, $\mathbf{z}$, arises in (4), which can be interpreted as a continuously distributed micromorphic force. An additional balance equation, which can be seen as a generalized angular momentum balance equation, connecting the skew part of $\boldsymbol{\sigma}$ with $\mathbf{S}$ and $\mathbf{z}$ is derived in the theory. In Appendix A, and after considering the HPFRC model that shall be presented in the following Section, we show that this equation trivially prescribes the symmetry of the stress tensor $\boldsymbol{\sigma}$.

The use of the Green theorem and the balance equations (3) and (4) in $P^{ext}$ establishes the identity: $P^{ext} = P^{\text{int}}$, where $P^{\text{int}}$ represents the total internal power and is given by:

$$P^{\text{int}} = \int_{\mathfrak{B}} (\boldsymbol{\sigma} : \nabla^s\dot{\mathbf{u}} + \mathbf{z}\cdot\dot{\boldsymbol{\beta}} + \mathbf{S} : \nabla\dot{\boldsymbol{\beta}})d\Omega \tag{5}$$

Notice that $\mathbf{z}$ and $\mathbf{S}$ play the role of generalized forces conjugate to $\dot{\boldsymbol{\beta}}$ and $\nabla\dot{\boldsymbol{\beta}}$, respectively.

### 2.3. Constitutive constraints

Next, we consider the material free energy density function: $\psi(\nabla^s\mathbf{u}, \boldsymbol{\beta}, \nabla\boldsymbol{\beta}, \boldsymbol{\alpha})$ where, for simplicity, the analysis is restricted to the isothermal case. The variable $\boldsymbol{\alpha}$ denotes the possible dependence of the constitutive response on a set of internal variables.

The isothermal version of the second law of thermodynamics prescribes, for any arbitrary deformation path, the verification of the inequality:

$$P^{\text{int}} - \dot{\psi} = (\boldsymbol{\sigma} : \nabla^s\dot{\mathbf{u}} + \mathbf{z}\cdot\dot{\boldsymbol{\beta}} + \mathbf{S} : \nabla\dot{\boldsymbol{\beta}}) - \dot{\psi} \geqslant 0. \tag{6}$$

which, after applying the Coleman's method, establishes the following identities for every one of the generalized forces:

$$\boldsymbol{\sigma} = \frac{\partial\psi}{\partial\nabla^s\mathbf{u}}; \quad \mathbf{S} = \frac{\partial\psi}{\partial\nabla\boldsymbol{\beta}}; \quad \mathbf{z} = \frac{\partial\psi}{\partial\boldsymbol{\beta}} \tag{7}$$

that are considered as constitutive constraints in the material model formulation.

## 3. HPFRC model using a multifield theory

### 3.1. Idealization of the fiber-matrix bond-slip mechanism

Fig. 2 sketches a representative specimen of HPFRC composite undergoing a loading process. The axial forces $\mathbf{P}$ are applied at both ends of the specimen. The mechanical description of the phenomena taking place at the mesostructural level, in this simple loading case, can be imagined as follows: the fiber is subjected to a cross sectional average axial stress $\bar{\sigma}_f$, while a circumferential average bond shear stress $\bar{\tau}_f$ arises in the interface zone between cement and fiber. The latter action has the effect of interconnecting the mechanical response of both components in order to make compatible the strains of fiber and matrix. Therefore, $\bar{\tau}_f$ is different from zero only if a relative displacement, slip motion, between fiber and cement occurs. The interface zone is here understood as a shell with zero thickness and is denoted $\Gamma$.

In order to take into account this mesoscopic phenomenon, we introduce a continuous microfield, $\boldsymbol{\beta}(\mathbf{x}, t)$, representing the relative displacement between fiber and matrix, i.e. the bond slip mechanism. In the context of a multifield theory, $\boldsymbol{\beta}$ represents the morphological descriptor of the model.

### 3.2. Hypotheses of the model

In order to derive the HPFRC composite model, the following hypotheses are adopted:

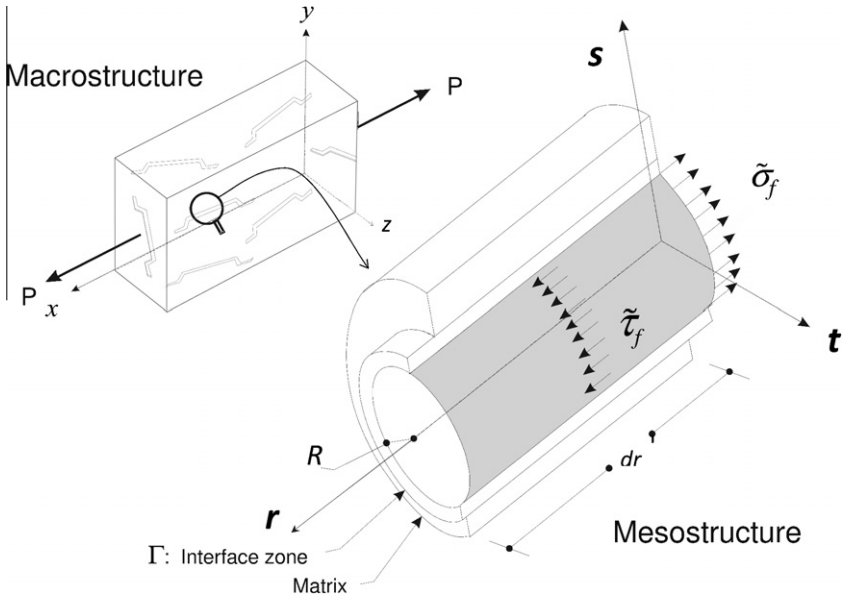


**Fig. 2.** Idealization of the fiber matrix bond-slip mechanism at the mesoscale level in a HPFRC composite.

i. small deformation theory and quasi static loading process shall be considered;
ii. each fiber does not interact with neighboring fibers nor a fiber bundle, in one direction, interacts with another bundle in a different direction;
iii. after initiation of cement cracking, the dowel effect induced by the fiber is neglected;
iv. the composite is defined as a homogeneous continuum in which each infinitesimal volume is occupied simultaneously by all the constituents, including fiber bundles in all directions existing in the composite, in a proportion given by the volume fraction of each component.

### 3.3. Configuration space and kinematical description of the composite

Let us consider a single fiber undergoing a tensile loading process, as depicted in Fig. 3a. Also, let us consider a local cartesian system, $(\mathbf{r}, \mathbf{s}, \mathbf{t})$, with the r-axis being parallel to the fiber. The present model assumes one local cartesian system for every fiber bundle direction in the bulk material.

Fig. 3b and c depicts the idealization of the fiber-matrix deformation mechanism, in a given Section A–A′ parallel to the plane $(\mathbf{s}, \mathbf{t})$. During the initial loading stage, Fig. 3b, it is assumed that both components, the matrix and the fiber, are perfectly joined, so that there is no slip between them. Thus, the same displacement $\bar{\mathbf{u}}$ describes the kinematics of the composite. Specifically, the r-component of the displacement vector: $\bar{u}_r$, is identical for both components. In this figure, the dashed thin lines are used to indicate the initial (undeformed) position of the Section A–A′, while the dot-dashed thick lines show the deformed position of the particles that initially were placed in A–A′.

As the tensile stress is increased, the bond shear strength is reached. Then, a second stage develops, as depicted in Fig. 3c, in which the pull out mechanism activates the progressive failure in

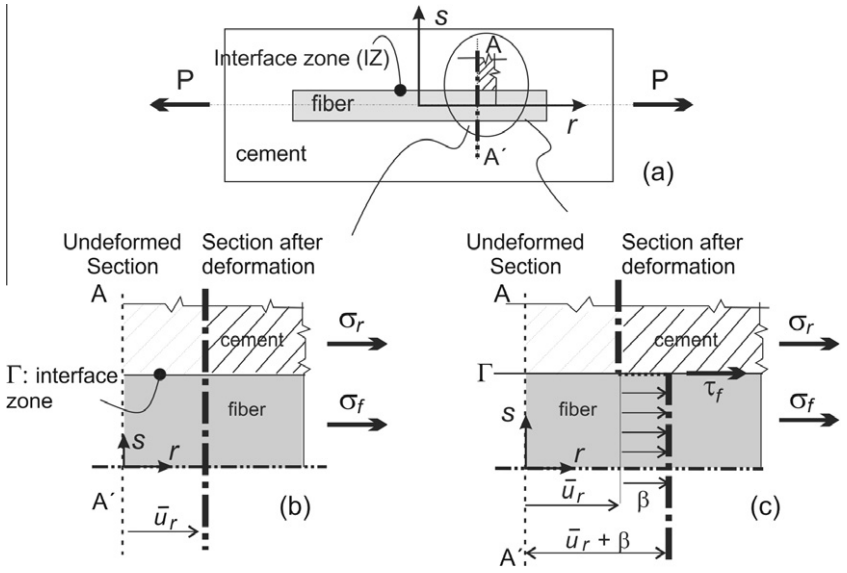


**Fig. 3.** Kinematics at the mesoscale level. (a) Unit cell depicting a steel fiber embedded into a cement volume element; (b) deformed Section A–A′ without matrix–fiber slip ($\beta = 0$); (c) deformed Section A–A′ with fiber–matrix slip ($\beta \neq 0$).

the interface zone, $\Gamma$, inducing a relative movement (slip) between the two phases.

While the matrix undergoes a displacement $\bar{\mathbf{u}}$, relative to the original position, the fiber displacement is: $\mathbf{u} = \bar{\mathbf{u}} + \boldsymbol{\beta}$. The relative fiber-matrix displacement is supposed to have only an axial component, in the fiber direction. Then, the vector $\boldsymbol{\beta}$ is:

$$\boldsymbol{\beta} = \beta(r,s,t)\mathbf{r} \tag{8}$$

which has a magnitude $\beta$ and is parallel to the vector $\mathbf{r}$.

Under this condition, the displacement field $\mathbf{u}(\mathbf{x})$ in the composite can be defined as follows:

$$\mathbf{u} = \bar{\mathbf{u}} + \mathcal{H}_f\beta; \quad \mathcal{H}_f \begin{cases} = 0 & \forall \mathbf{x} \text{ in the concrete domain} \\ = 1 & \forall \mathbf{x} \text{ in the fiber domain} \end{cases} \tag{9}$$

where $\mathcal{H}_f$ denotes the Heaviside step function and defines in what points of the body, the slip displacement $\boldsymbol{\beta}$ is different from zero.

From now on, and without loss of generality, only 2D problems with plane symmetry described in the plane $(\mathbf{r},\mathbf{s})$ are addressed; the geometry of the steel fiber reinforcement is assumed such that it preserves this symmetry. Then, $\nabla\boldsymbol{\beta}$ is given by:

$$\nabla\boldsymbol{\beta} = \beta_{,r}(\mathbf{r}\otimes\mathbf{r}) + \beta_{,s}(\mathbf{r}\otimes\mathbf{s}) \tag{10}$$

where the notation $(\cdot)_{,r} = \partial(\cdot)/\partial r$ and $(\cdot)_{,s} = \partial(\cdot)/\partial s$ is used.

From expression (9), the strain is:

$$\begin{aligned}\boldsymbol{\varepsilon} &= \nabla^s\mathbf{u} = \nabla^s\bar{\mathbf{u}} + \delta_\Gamma(\boldsymbol{\beta}\bar{\otimes}^s\mathbf{s}) + \mathcal{H}_f(\nabla^s\boldsymbol{\beta}) \\ &= \nabla^s\bar{\mathbf{u}} + \delta_\Gamma\beta(\mathbf{r}\bar{\otimes}^s\mathbf{s}) + \mathcal{H}_f(\beta_{,r}(\mathbf{r}\bar{\otimes}^s\mathbf{r}) + \beta_{,s}(\mathbf{r}\bar{\otimes}^s\mathbf{s}))\end{aligned} \tag{11}$$

where the supra-index $(\cdot)^s$ refers to the symmetric part of the corresponding second order tensor. The second term in the right hand side is obtained after using the generalized gradient: $\nabla\mathcal{H}_f = \delta_\Gamma\mathbf{s}$, with $\delta_\Gamma$ being the Dirac delta function shifted to $\Gamma$ (the fiber–matrix interface surface). Thus, the strain in the matrix (where $\mathcal{H}_f = 0$) is:

$$\boldsymbol{\varepsilon}_m = \nabla^s\bar{\mathbf{u}}; \tag{12}$$

while, the fiber strain results:

$$\boldsymbol{\varepsilon}_f = \mathcal{H}_f(\nabla^s\bar{\mathbf{u}} + \beta_{,r})(\mathbf{r}\otimes\mathbf{r}) + \beta_{,s})(\mathbf{r}\bar{\otimes}^s\mathbf{s}) \tag{13}$$

and the remaining term in equation (11):

$$\boldsymbol{\gamma} = \delta_\gamma\beta(\mathbf{r}\bar{\otimes}^s\mathbf{s}) \tag{14}$$

can be interpreted as a singular shear strain concentrated in the interface surface.

### 3.4. HPFRC constitutive equations

In this section, the HPFRC constitutive model is presented according to the following guidelines. First, in Section 3.4.1, we introduce the basic description of the free energy, and its partition into different terms, associated with every component of the composite producing power in the mechanical idealization, sketched in Fig. 2, at the mesoscale level. Furthermore, at this point, we define the very important notion of how each of these partitions depend on the kinematical variables defining the body configuration. In the next Section 3.4.2, after adopting the basic definitions given in Section 3.4.1 and using the constitutive constrains (7), we interpret the stress associated with each component, as also, the microstresses and microforces concepts arising in the micromorphic model. Finally, in Section 3.4.3, we specify the constitutive model of each component, and the overall constitutive model of the composite (Section 3.4.4), in agreement with the generic expression adopted for the free energy in the first Section 3.4.1 and the expression derived in Section 3.4.2.

The concepts addressed in Sections 3.4.1–3.4.3 are developed supposing the existence of only one fiber bundle, with a single fiber orientation. The overall model in Section 3.4.4 is then generalized to account for a number of arbitrary fiber orientations.

#### 3.4.1. Composite free energy according to the mixture theory

According to the hypothesis (iv) of Section 3.2, the hypothesis of the mixture theory is taken in order to derive the expression of the composite free energy. Instead of characterizing the whole composite performance, the mixture theory focuses on modeling each component separately. The classical mixture theory has been modified since its appearance in 1960 (Trusdell and Toupin, 1960), to include non-linearity in the constitutive response of the components (Oller et al., 1996; Car et al., 2002).

Let us first consider a unique fiber bundle oriented in the direction $\mathbf{r}$. We denote $k_f$ the volume fraction of the fiber, and $k_m$ the volume fraction of the cement matrix, such that: $k_f + k_m = 1$.

The free energy of the composite is defined as follows:

$$\begin{aligned}\psi(\nabla^s\bar{\mathbf{u}},\boldsymbol{\beta},\nabla\boldsymbol{\beta},\boldsymbol{\alpha}) = {} & k_m\psi_m(\boldsymbol{\varepsilon}_m(\nabla^s\bar{\mathbf{u}}),\alpha_m) \\ & + k_f\psi_f(\boldsymbol{\varepsilon}_f(\nabla^s\bar{\mathbf{u}},\nabla\boldsymbol{\beta}),\alpha_f) + k_f\delta_\gamma\bar{\psi}_\Gamma(\boldsymbol{\beta},\alpha_\Gamma)\end{aligned} \tag{15}$$

where $\psi_m$ and $\psi_f$ are the matrix and fiber free energies, respectively. As we have shown above, the matrix–fiber bond is subjected to interaction forces producing power. In the present model, we characterize this mechanism by including an additional term in the free energy expression, which is given by the surface free energy: $\bar{\psi}_\Gamma$ at the interface. The Dirac delta function $\delta_\Gamma$ expresses the fact that $\bar{\psi}_\Gamma$ is a surface energy density in $\Gamma$. Notice that each term of the free energy has its own set of internal variables: $\alpha_m$, $\alpha_f$ and $\alpha_\Gamma$, respectively.

Every term of the total free energy in (15) is defined as follows:

(i) The brittle behavior of the matrix is characterized by a tensile/compressive continuum isotropic damage model in the context of a smeared crack approach. The matrix free energy is given by:

$$\psi_m(\boldsymbol{\varepsilon}_m(\nabla^s\bar{\mathbf{u}},\alpha_m)) = \frac{1}{2}(1-d_m)(\boldsymbol{\varepsilon}_m : \mathbb{C}_m : \boldsymbol{\varepsilon}_m) \tag{16}$$

where $d_m \in [0,1]$, is the conventional damage variable describing the degradation of the elastic stiffness: $d_m = 0$ represents the virgin material and $d_m = 1$ the completely degraded material. The evolution equation for $d_m$ is presented in the next Section. The matrix strain, $\boldsymbol{\varepsilon}_m$, is defined in (12), and $\mathbb{C}_m$ is the standard isotropic elastic tensor.

(ii) The steel fiber is modeled using a one-dimensional plastic model with strain hardening/softening response. Its free energy is characterized by:

$$\begin{aligned}\psi_f(\boldsymbol{\varepsilon}_f(\nabla^s\bar{\mathbf{u}},\nabla\boldsymbol{\beta}),\alpha_f) = {} & \frac{1}{2}(\boldsymbol{\varepsilon}_f^e : \mathbb{E}_f : \boldsymbol{\varepsilon}_f^e) + \psi_f^h(\alpha_f); \\ & \mathbb{E}_f = E_f(\mathbf{r}\otimes\mathbf{r})\otimes(\mathbf{r}\otimes\mathbf{r})\end{aligned} \tag{17}$$

where we have assumed that the total fiber strain $\boldsymbol{\varepsilon}_f$, defined in (13), splits additively into an elastic, $\boldsymbol{\varepsilon}_f^e$, and a plastic, $\boldsymbol{\varepsilon}_f^p$, parts:

$$\boldsymbol{\varepsilon}_f = \boldsymbol{\varepsilon}_f^e + \boldsymbol{\varepsilon}_f^p. \tag{18}$$

the elasticity tensor, $\mathbb{E}_f$, is defined by only one elastic modulus: $E_f$, as shown in (17)-b, and $\psi_f^h$ is the free energy partition associated with the hardening/softening mechanism which depends on the scalar internal variable: $\alpha_f$. The function $\psi_f^h$, as well as the evolution equations for $\boldsymbol{\varepsilon}_f^p$, $\alpha_f$ are defined in the next sections.

(iii) The constitutive response of the interface $\Gamma$ is characterized by an elasto-plastic frictional cohesive model with strain hardening/softening. Its surface free energy is described by:

$$\begin{aligned}\bar{\psi}_\Gamma(\boldsymbol{\beta},\alpha_\Gamma) = {} & \frac{1}{2}(\boldsymbol{\beta}^e\cdot\mathbb{G}_\Gamma\cdot\boldsymbol{\beta}^e) + \bar{\psi}_\Gamma^h(\alpha_\Gamma) \\ & \mathbb{G}_\Gamma = G_\Gamma(\mathbf{r}\otimes\mathbf{r})\end{aligned} \tag{19}$$

where $\boldsymbol{\beta}$ is assumed to be the addition of an elastic part $\boldsymbol{\beta}^e$ and a plastic part $\boldsymbol{\beta}^p$:

$$\boldsymbol{\beta} = \boldsymbol{\beta}^e + \boldsymbol{\beta}^p \tag{20}$$

the second order stiffness tensor, $\mathbb{G}_\Gamma$, is defined by means of only one stiffness modulus: $G_\Gamma$ (a very large penalty-like parameter with dimension: [N/m] and which penalizes the fiber/matrix slip before a certain stress threshold is reached). The partition: $\bar{\psi}_\Gamma^h$ of the surface free energy, is associated with the strain hardening/softening effect due to the frictional mechanism in the bond and depends on the scalar internal variable $\alpha_\Gamma$. The evolution equation for: $\boldsymbol{\beta}^p$ and $\alpha_\Gamma$, as well as the definition of $\bar{\psi}_\Gamma^h$, are shown in the following section.

### 3.4.2. Generalized forces arising in the micromorphic model

From the above free energy expressions, the strains of all components (Eqs. (11)–(14)) and the constitutive constraints (7)-a; the conventional Cauchy stress is given by:

$$\begin{aligned}\boldsymbol{\sigma} &= \frac{\partial \psi}{\partial \nabla^s \bar{\mathbf{u}}} = k_m \frac{\partial \psi_m}{\partial \nabla^s \bar{\mathbf{u}}} + k_f \frac{\partial \psi_f}{\partial \nabla^s \bar{\mathbf{u}}} = k_m(1-d_m)(\mathbb{C}_m : \boldsymbol{\varepsilon}_m) + k_f \mathbb{E}_f : \boldsymbol{\varepsilon}_f^e \\ &= k_m(1-d_m)(\mathbb{C}_m : \boldsymbol{\varepsilon}_m) + \underbrace{k_f E_f((\bar{u}_r)_{,r} + \beta_{,r})^e}_{\sigma_f}(\mathbf{r}\otimes\mathbf{r}) = k_m \boldsymbol{\sigma}_m + k_f \boldsymbol{\sigma}_f\end{aligned} \tag{21}$$

where we have replaced the expressions of $\boldsymbol{\varepsilon}_f^e$ and $\mathbb{E}_f$ given in (13) and (17)-2, respectively. Also, we identify $\boldsymbol{\sigma}_m$ as the cement matrix stress and $\boldsymbol{\sigma}_f$ as the (uniaxial) fiber stress:

$$\boldsymbol{\sigma}_m = (1-d_m)\mathbb{C}_m : \boldsymbol{\varepsilon}_m \tag{22}$$

$$\boldsymbol{\sigma}_f = \sigma_f(\mathbf{r}\otimes\mathbf{r}) = E_f((\bar{u}_r)_{,r} + \beta_{,r})^e(\mathbf{r}\otimes\mathbf{r}) \tag{23}$$

Considering expressions (7)-b, (13) and (17), the microstress $\mathbf{S}$ is given by:

$$\begin{aligned}\mathbf{S} &= \frac{\partial \psi}{\partial \nabla \beta} = k_f \frac{\partial \psi_f}{\partial \nabla \beta} = \mathcal{H}_f(k_f \mathbb{E}_f \cdot \varepsilon_f^e) \\ &= \mathcal{H}_f k_f E_f((\bar{u}_r)_{,r} + \beta_{,r})^e(\mathbf{r}\otimes\mathbf{r}) = \mathcal{H}_f k_f \boldsymbol{\sigma}_f\end{aligned} \tag{24}$$

where, from the intermediate identity and (21), we recognize that $\mathbf{S}$ is represented by $\boldsymbol{\sigma}_f$ in the fiber domain (weighted by the fiber volume fraction) and zero in the remaining part of the volume. Observe that $\mathbf{S}$, in components referred to the cartesian system $(\mathbf{r}, \mathbf{s})$, is given by:

$$\mathbf{s} = \mathcal{H}_f k_f \begin{bmatrix} \sigma_f & 0 \\ 0 & 0 \end{bmatrix}. \tag{25}$$

From expressions (7)-c, and (15), the micromorphic force results:

$$\mathbf{z} = \frac{\partial \psi}{\partial \boldsymbol{\beta}} = k_f \delta_\Gamma \frac{\partial \bar{\psi}_\Gamma}{\partial \beta} = \delta_\Gamma(k_f \mathbb{G}_\Gamma \cdot \boldsymbol{\beta}^e) = \delta_\Gamma(k_f G_\Gamma \beta^e)\mathbf{r} = \delta_\Gamma(k_f \tau_f)\mathbf{r} \tag{26}$$

which can be rewritten as: $\mathbf{z} = \delta_\Gamma \bar{\mathbf{z}}$. Thus, we identify $\bar{\mathbf{z}} = k_f(G_\Gamma \beta^e)\mathbf{r}$ as a specific shear force per unit of area (a traction vector) acting in the interface being the shear stress component: $\tau_f$, defined by:

$$\tau_f = G_\gamma \beta^e, \tag{27}$$

in the direction of $\mathbf{r}$ and weighted by the fiber volume fraction. Expression (27) can be reinterpreted as a conventional cohesive interface traction-separation model arising in the interface.

### 3.4.3. Additional ingredients of the constitutive equation

The evolution equations for the internal variables, as well as the remaining ingredients of the constitutive model in each component of the HPFRC, are defined in the following items.

#### 3.4.3.1. Damage model for cement with distinct tensile and compressive strengths.

The equations of the isotropic continuum damage model for cement are summarized in the Box 1. This model is based on the approach adopted by Oliver et al. (2008), Linero (2006), Linero et al. (2010), for concrete, where the conventional continuum damage variable $d_m$ is reinterpreted in terms of the ratio between two conjugate internal variables of the model, $q_m$ and, $r_m$, which are the stress-like and strain-like internal variables respectively, as shown in equation (29). After replacing (29) in (22), we obtain the stress–strain relation (30).

Box 1. Tensile/compressive isotropic damage model.

Free energy : $$\psi_m(\boldsymbol{\varepsilon}_m(\nabla^s \bar{\mathbf{u}}), \alpha_m) = \frac{1}{2}(1-d_m)(\boldsymbol{\varepsilon}_m : \mathbb{C}_m : \boldsymbol{\varepsilon}_m) \tag{28}$$

Damage variable : $$d_m = 1 - \frac{q_m}{r_m} \tag{29}$$

Stress–strain relation : $$\boldsymbol{\sigma}_m = \frac{q_m}{r_m}(\mathbb{C}_m : \boldsymbol{\varepsilon}_m) \tag{30}$$

Flow rule : $$\dot{r}_m = \lambda_m, \quad r_m \geqslant r_0 \tag{31}$$

Internal variable evolution : $$r_m = \max_{s\in[0,t]}[r_0, \tau_\varepsilon(\boldsymbol{\varepsilon}_m(s))]; \quad r_m|_{t=0} = r_0 = \frac{\sigma_m^{ut}}{\sqrt{E_m}} \tag{32}$$

Damage criterion : $$f_m(\boldsymbol{\varepsilon}_m, r_m) = \tau_\varepsilon - r_m \tag{33}$$

Isotropic hardening law : $$\dot{q}_m = H_m(r_m)\dot{r}_m; \quad 0 \leqslant q_m \leqslant r_0; \quad q_m|_{t=0} = r_0 \tag{34}$$

Complementary conditions : $$f_m \leqslant 0; \quad \lambda_m \geqslant 0; \quad \lambda_m f_m = 0 \tag{35}$$

Expression (31) defines the evolution equation for $r_m$, where $\lambda_m$ is a positive damage multiplier, which is not null only if the strain state lies on the surface $f_m = 0$, with $f_m$ being defined in (33). $E_m$ is the Young modulus of cement and $\sigma_m^{ut}$ is the elastic uniaxial tensile strength.

The damage function (33) is expressed in terms of the matrix effective stress: $\bar{\boldsymbol{\sigma}}_m = \mathbb{C}_m : \boldsymbol{\varepsilon}_m$. The term $\tau_\epsilon$ for the damage model with distinct tensile and compressive strengths, is defined as follows:

$$\tau_\varepsilon = (\theta + \frac{1-\theta}{n})\sqrt{\bar{\boldsymbol{\sigma}}_m : (\mathbb{C}_m)^{-1} : \bar{\boldsymbol{\sigma}}_m}, \quad \text{with :} \quad \theta = \frac{\sum_{i=1}^3 \langle \bar{\sigma}_m^i \rangle}{\sum_{i=1}^3 |\bar{\sigma}_m^i|} \tag{36}$$

where $\langle\cdot\rangle$ denotes the Mac Auley bracket. $\bar{\sigma}_m^i$ is the $i$-th principal stress of $\bar{\boldsymbol{\sigma}}_m$ and $n = \sigma_m^{uc}/\sigma_m^{ut}$, where $\sigma_m^{uc}$ is the uniaxial elastic compressive strength. Typical values for standard concrete are: $n \simeq 10$. Also, observe that considering $\mathbb{C}_m$ as a metric tensor, $\tau_\varepsilon$ can be seen as a strain norm that is scaled by the dimensionless coefficient: $(\theta + \frac{1-\theta}{n})$. The elastic domain: $f_m \leqslant 0$, in the principal stress space, is plotted in Fig. 4a, as well as, a typical uniaxial stress–strain curve representing the behavior of the present concrete model. Notice in the plot, the different values displayed by the maximum compressive and tensile strengths, respectively.

Expression (34) is the so-called hardening/softening law relating the thermodynamic force $q_m$ with the conjugate variable

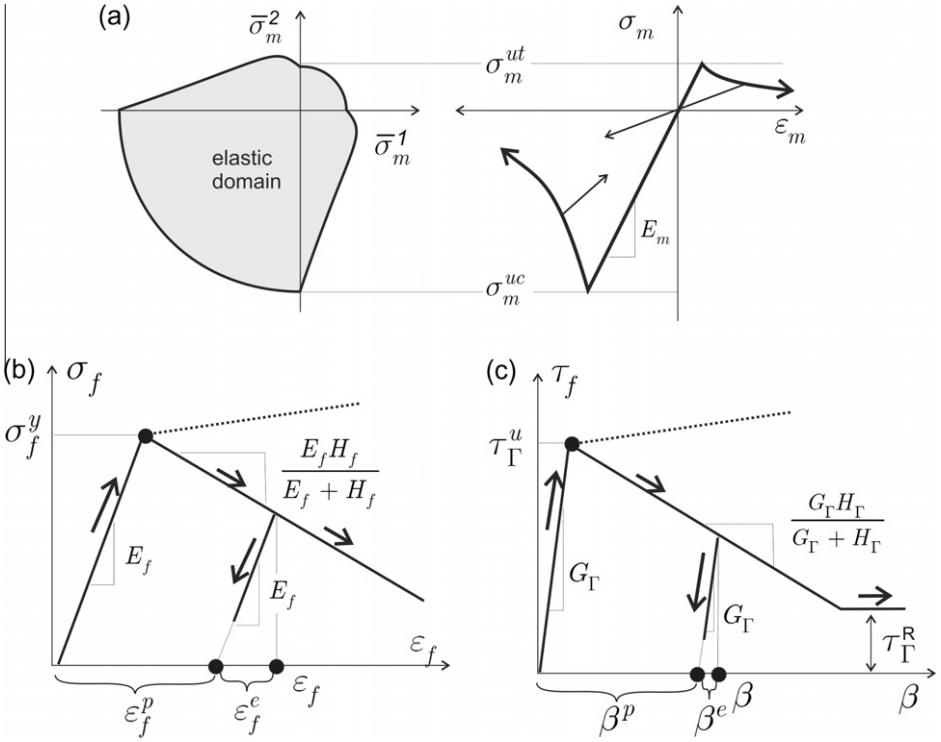


**Fig. 4.** Constitutive model of the HPFRC components. (a) Cement matrix model, description of the 2D elastic domain in the principal stress space (left) and uniaxial stress vs. strain plot (right); (b) fiber model and (c) cohesive interface model representing the fiber–matrix bond response.

$r_m \cdot H_m$ is the softening modulus which is regularized in term of the concrete fracture energy: $G_{m_f}$ and the size of the finite element (Oliver et al. 2010).

The constitutive tangent tensor: $\mathbb{C}_m^{tg} = \partial \boldsymbol{\sigma}_m / \partial \boldsymbol{\varepsilon}_m$ of the proposed damage model is given by the following expressions:

$$\mathbb{C}_m^{tg} = \frac{q_m}{r_m}\mathbb{C}_m;$$
$$\mathbb{C}_m^{tg} = \frac{q_m}{r_m}\mathbb{C}_m + \frac{H_m r_m - q_m}{(r_m)^3}\left(\frac{(r_m)^2}{\theta}[\bar{\boldsymbol{\sigma}}_m \otimes (\mathbb{C}_m : \partial_{\boldsymbol{\sigma}}\theta) + \theta^2(\bar{\boldsymbol{\sigma}}_m \otimes \bar{\boldsymbol{\sigma}}_m)]\right) \tag{37}$$

Eq. (37)-a corresponds to unloading conditions and (37)-b to loading conditions. See additional details in Oliver et al. (2008) and Linero (2006), where the expression for $\partial_{\boldsymbol{\sigma}}\theta$ has been derived.

*3.4.3.2. Plastic behavior of the fiber oriented in the r direction.* As it was advanced in Eq. (21), the additional ingredients of the constitutive relation connecting the uniaxial fiber stress: $\sigma_f = \boldsymbol{\sigma}_f : (\mathbf{r}\otimes\mathbf{r})$ with the uniaxial fiber strain: $\varepsilon_f = \boldsymbol{\varepsilon}_f : (\mathbf{r}\otimes\mathbf{r}) = (\bar{u}_r)_{,r} + \beta_{,r}$, where $\boldsymbol{\varepsilon}_f$ is defined in equation (13), are here presented. To connect both magnitudes, we propose an uniaxial standard elasto-plastic stress–strain model as it is presented in Box 2, see also Fig. 4b. The fiber strain: $\varepsilon_f$, is supposed to be partitioned in the addition of an elastic $\varepsilon_f^e$, and plastic part $\varepsilon_f^p$ ($\varepsilon_f = \varepsilon_f^e + \varepsilon_f^p$).

The stress $\sigma_f$ is linearly connected with the elastic part: $\varepsilon_f^e$ of the fiber strain, as shown in equation (39) where $E_f$ is the fiber Young's modulus. Eq. (39) is the scalar expression of the fiber tensorial term given in (21).

The plastic strain rate $\dot{\varepsilon}_f^p$, equation (40), is defined through a standard uniaxial plastic response, while $\lambda_f$ is the plastic multiplier. The pair $(\alpha_f, q_f)$ is the set of conjugate internal variables, and $H_f = \partial^2\psi_f^h/\partial\alpha_f^2$ is the hardening/softening modulus. The yield surface, $f_f$ is defined in (43), where $\sigma_f^y$ represents the fiber yield stress. Expressions (44) are the classical plastic loading–unloading conditions.

Box 2.1-D plastic model for a fiber oriented in the **r** direction.

Free energy : $\psi_f(\boldsymbol{\varepsilon}_f(\nabla^s\bar{\mathbf{u}}, \nabla\boldsymbol{\beta}), \boldsymbol{\alpha}_f) = \frac{1}{2}E_f[\varepsilon_f^e]^2 + \psi_f^h(\alpha_f)$ (38)

Elastic stress—strain relationship : $\sigma_f = E_f\varepsilon_f^e$ (39)

Flow rule : $\dot{\varepsilon}_f^p = \lambda_f sign(\sigma_f)$ (40)

Internal variable evolution : $\dot{\alpha}_f = \lambda_f; \quad \alpha_f|_{t=0} = 0$ (41)

Isotropic hardening law : $\dot{q}_f = H_f(\alpha_f)\dot{\alpha}_f; \quad q_f \in [-\sigma_f^y; 0]$ (42)

Yield condition : $f_f = |\sigma_f| - (q_f + \sigma_f^y)$ (43)

Complementary conditions : $f_f \leqslant 0; \quad \lambda_f \geqslant 0; \quad \lambda_f f_f = 0$ (44)

The elastoplastic tangent modulus: $\mathbb{C}_f^{tg} = \partial\boldsymbol{\sigma}_f/\partial\boldsymbol{\varepsilon}_f$, is given by:

$$\mathbb{C}_f^{tg} = E_f[(\mathbf{r}\otimes\mathbf{r})\otimes(\mathbf{r}\otimes\mathbf{r})]; \quad \text{for unloading conditions}$$
$$\mathbb{C}_f^{tg} = \frac{E_f H_f}{E_f + H_f}[(\mathbf{r}\otimes\mathbf{r})\otimes(\mathbf{r}\otimes\mathbf{r})]; \quad \text{for loading conditions} \tag{45}$$

*3.4.3.3. Constitutive equations for the (cohesive) interface zone: bond stress–slip relationship.* In equation (27), a cohesive interface model has been introduced:

$\tau_f = \hat{\tau}(\beta)$, representing the mechanical behavior in the interface zone $\Gamma$. In this Section, we present the additional ingredients defining completely this frictional constitutive relation.

Due to the notable effect that the matrix–fiber bond strength value, as well as the evolution of the debonding process, has on the macroscopic behavior of HPFRC composites, this phenomena has been widely analyzed in the literature, mainly through pull-out experimental tests; such as the studies presented in Naaman et al. (1991a), Shannag et al. (1999), Li and Stang (1997). Recent researches have contributed to the optimization of the fiber geometrical properties to increase the bond strength (Naaman, 2003). While several bond strengths values for smooth, hooked end and twisted fibers are given in Kim et al. (2009).

We assume that the interfacial zone mechanical response follow a one-dimensional elasto-plastic traction-slip model, as shown in Box 3. In Fig. 4c, we sketch the main parameters characterizing the constitutive response of this component.

Box 3.1-D plastic model for the interface zone ($\Gamma$).

Specific free energy : $\bar{\psi}_\Gamma(\beta^e, \alpha_\Gamma) = \frac{1}{2}(\beta^e \cdot G_\Gamma \cdot \beta^e) + \bar{\psi}^h_\Gamma(\alpha_\Gamma)$ (46)

Elastic stress – strain relationship : $\tau_f = G_\Gamma \beta^e$ (47)

Flow rule : $\dot{\beta}^p = \lambda_\Gamma sign(\tau_f)$ (48)

Internal variable evolution : $\dot{\alpha}_\Gamma = \lambda_\Gamma; \quad \alpha_\Gamma|_{t=0} = 0$ (49)

Yield condition : $f_\Gamma(\tau_f, \alpha_\Gamma) = |\tau_f| - (q_\Gamma + \tau^u_\Gamma)$ (50)

Isotropic hardening law : $\dot{q}_\Gamma = H_\Gamma(\alpha_\Gamma)\dot{\alpha}_\Gamma; \quad q_\Gamma \in [-(\tau^u_\Gamma - \tau^R_\Gamma); 0]$ (51)

Complementary conditions : $f_\Gamma \leqslant 0; \quad \lambda_\Gamma \geqslant 0; \quad \lambda_\Gamma f_\Gamma = 0$ (52)

The model in Box 3 basically consists of a linear-elastic response between the elastic partition of $\beta$ defined as: $\beta^e = \beta - \beta^p$ and $\tau_f$. Both terms are related through a very large stiffness modulus (a penalty-like parameter): $G_\Gamma$; up to reach the bond strength value: $\tau^u_\Gamma$, which characterizes, for the virgin material, the onset of the inelastic process. This parameter determines the stick strength of the bond-slip model. After crossing this point, the bond-slip response follows a plastic hardening/softening rule. Thus, the evolution of the plastic component: $\beta^p$ is given by the flow law (48), where $\lambda_\Gamma$ (with dimension of length) represents the plastic multiplier. The hardening/softening rule is defined by the expressions (49) and (51), where the term: $H_\Gamma$ (with dimension: [N/m]) represents the instantaneous hardening/softening modulus. The plasticity criterion is given by the equation: $f_\Gamma = 0$, with $f_\Gamma$ defined in (50). And the loading–unloading conditions by (52). The parameter $\tau^R_\Gamma$ defines a residual frictional strength, allowing more realistic capturing responses in the fiber–matrix interaction model. This residual strength could be the reason of displaying post-peak structural behaviors with long tails, which are usually observed in HPRFC specimens.

The elasto-plastic tangent modulus: $C^{tg}_\Gamma = \partial\tau_f/\partial\beta$, is given by:

$$C^{tg}_\Gamma = G_\Gamma; \quad \text{for unloading conditions}$$
$$C^{tg}_\Gamma = \frac{G_\Gamma H_\Gamma}{G_\Gamma + H_\Gamma}; \quad \text{for loading conditions} \tag{53}$$

*3.4.4. The overall constitutive model of HPFRC composite having a random distribution of fiber directions.*

The previously presented mechanical model of a HPRFC, having a fiber bundle in one direction, can be generalized to account for a statistical distribution of fibers. Let us consider $n_f$ discrete fiber bundles in the plane of analysis with a regular distribution of angles in the interval: $[0, \pi]$.

The $i$-th bundle, characterized with the supra-index $I$, $(I = 1, \ldots, n_f)$, has assigned one volume fraction $k^I_f$, one direction vector $\mathbf{r}^I$ and one micromorphic field $\boldsymbol{\beta}^I = \beta^{(I)}(r,s)\mathbf{r}^{(I)}$ (from now on, a supra-index in parenthesis indicates that no summation on that index is implied). Inclusion of new micromorphic fields implies that new associated microstresses $\mathbf{S}^I$ and microforces $\mathbf{z}^I$ arise for every considered index $I$. Also, it is required the fulfillment of an additional balance equation (4) for every index $I$.

Using the mixture theory, the free energy of the HPFRC is the linear combination of free energies of all the components weighted by their corresponding volume fraction. Then, the stress equation (21) results:

$$\boldsymbol{\sigma} = k_m \boldsymbol{\sigma}_m(\boldsymbol{\varepsilon}_m; \alpha_m) + \sum_{I=1}^{n_f} k^I_f \boldsymbol{\sigma}^I_f(\varepsilon^I_f(\bar{\mathbf{u}}, \boldsymbol{\beta}^I); \alpha^I_f) \tag{54}$$

where $\boldsymbol{\sigma}^I_f$ corresponds to the $i$-th fiber stress, which expression is given by the last term in (21) along the direction $\mathbf{r}^I$. Notice that the bond shear stress $\tau_f$, determined with Box 3, is not included in this equation. The tangent constitutive tensor: $\mathbb{C}^{tg} = \partial\boldsymbol{\sigma}/\partial\boldsymbol{\varepsilon}$, is given by:

$$\mathbb{C}^{tg} = k_m \mathbb{C}^{tg}_m + \sum_{I=1}^{n_f} k^I_f E^I_f [(\mathbf{r}^I \otimes \mathbf{r}^I) \otimes (\mathbf{r}^I \otimes \mathbf{r}^I)] \tag{55}$$

where $E^I_f$ is the Young's modulus of the $i$-th fiber bundle.

Furthermore, each fiber bundle $I$ has assigned a constitutive relation: $\sigma^I_f = \hat{\sigma}^I_f(\varepsilon^I_f, \alpha^I_f)$ and: $\tau^I_f = \hat{\tau}^I_f(\beta^I, \alpha^I_\Gamma)$, given by Box 2 and Box 3. In the remaining part of the paper, we will denote:

$$\boldsymbol{\sigma} = \hat{\boldsymbol{\sigma}}(\mathbf{u}, \boldsymbol{\beta}, \nabla\boldsymbol{\beta}, \boldsymbol{\alpha}); \quad \sigma_f = \hat{\sigma}_f(\varepsilon_f, \alpha_f); \quad \tau_f = \hat{\tau}_f(\beta, \alpha_\Gamma) \tag{56}$$

the complete set of the composite model constitutive equations. In this context, it is understood that notation: $\boldsymbol{\beta}$ and $\nabla\boldsymbol{\beta}$, as well as the functions: $\hat{\sigma}_f$ and $\hat{\tau}_f$, represent the set of micromorphic fields associated with all the fiber bundles, with indices: $I = 1, \ldots, n_f$.

## 4. BVP and variational formulation

### 4.1. Interpretation of the microforce balance law

To understand more precisely the role played by the microforce balance law (4) and considering that $\mathbf{S}$ and $\mathbf{z}$ are defined in the fiber and interface regions, respectively, it is more natural to consider an integral expression of that balance equation. Let us integrate this expression in the body part $\mathfrak{B}_B$ coinciding with the cylindrical slice of length $dr$, enclosing a fiber, and its associated interface surface, such as shown in the insert of Fig. 2 denoted "mesostructure". The integral expression results:

$$\int_{\mathfrak{B}_B}(\nabla\cdot\mathbf{S}-\mathbf{z})d\Omega=\begin{bmatrix}\int_{\Omega_f}((\sigma_f)_{,r})d\Omega_f\\0\end{bmatrix}-\begin{bmatrix}\int_\Gamma \tau_f d\Gamma\\0\end{bmatrix}=\begin{bmatrix}0\\0\end{bmatrix}\tag{57}$$

where the second identity is derived, after replacing equations (25) and (26) in the left part of (57), by performing simple mathematical operations. As it can be seen, the second component of the vector equation is trivially equal to zero. Thus, the relevant balance equation comes from the first component. Notice that, due to the presence of the Heaviside function in (25), the integration domain of the first term is restricted to the fiber volume, here denoted $\Omega_f$, while the integration domain in the second term is the surface, $\Gamma$, due to the Dirac delta function in (26).

Denoting $\tilde{\sigma}_f$ the average value of $\sigma_f$ in a given section of the fiber and $\tilde{\tau}_f$ the circumferential average in $\Gamma$ of the shear stress: $\tau_f$; the equation of the first component in expression (58) can be alternatively written as:

$$\tilde{\tau}_f-\frac{A_f}{\Pi_f}(\tilde{\sigma}_f)_{,r}=0\tag{58}$$

where $A_f$ and $\Pi_f$ are the cross-section area and the perimeter of the fiber, respectively. A similar equation describing the relation between the axial stress and the shear stress distribution at the interface zone was presented by Naaman et al. (1991a,b).

As it was mentioned above, there is one balance equation (58) for every fiber bundle which is characterized by the direction vector $\mathbf{r}^I$.

### 4.2. Reinterpretation of the fiber and bond constitutive models by means of averaged quantities

In view of the treatment given to the microforce balance law, equation (58), in terms of averaged quantities of the fiber and bond shear stresses, the constitutive relation in Box 2 and Box 3 should be reinterpreted such that the model in these boxes provides the averaged terms required in the balance equation.

We note that the kinematics description of the model assumes that fibers are one-dimensional geometrical entities, which means that the fiber displacement and the fiber strain $\varepsilon_f$, are implicitly considered as constant fields across the fiber section. Then, $\varepsilon_f\equiv\tilde{\varepsilon}_f$ (where $\tilde{\varepsilon}_f$ is the average strain value in a fiber cross section). Thus, provided that parameters are understood as averaged values, the constitutive model in Box2 automatically gives an averaged stress value $\tilde{\sigma}_f$ in the fiber cross-section, which depends on the averaged values of the fiber strain, $\tilde{\varepsilon}_f$, and the internal variable, $\tilde{\alpha}_f(\tilde{\sigma}_f=\hat{\tilde{\sigma}}_f(\tilde{\varepsilon}_f,\tilde{\alpha}_f))$. An identical consideration is valid for the constitutive relation given in Box 3, between the average bond shear stress $\tilde{\tau}_f$ in a circumferential line, and the slip $\beta$ and average internal variable $\tilde{\alpha}_\Gamma$ , through: $\tilde{\tau}_f=\hat{\tilde{\tau}}_f(\beta,\tilde{\alpha}_\Gamma)$.

### 4.3. Governing equations of the BVP

The balance equations (3) and (58) jointly with the constitutive equations (56) and the conventional traction boundary terms: $\boldsymbol{\sigma}\cdot\mathbf{n}=\mathbf{t}^*$, defined in $\partial\mathfrak{B}_\sigma$, or displacements: $\mathbf{u}=\mathbf{u}^*$, defined in $\partial\mathfrak{B}_u$, together with the prescription: $\boldsymbol{\beta}=\mathbf{0}$ in the complete body boundary $\partial\mathfrak{B}_\beta$ (with $\partial\mathfrak{B}_\beta=\partial\mathfrak{B}=\partial\mathfrak{B}_\sigma\cup\partial\mathfrak{B}_u$), define the boundary value problem in the strong form. These equations, that are written in terms of the macro-displacements $\mathbf{u}$ and the microslip, $\boldsymbol{\beta}$, are summarized in Box 4.

Note that an alternative possibility to prescribe a perfect fiber-matrix bond on the body surface ($\beta^I=0$ on $\partial\mathcal{B}$), is to defined a null fiber stress ($\tilde{\sigma}_f^I=0$) on $\partial\mathcal{B}$. Both possibilities are amenable to motivate pros and cons. Nevertheless, as it is observed in the numerical simulation to be presented in next Section, the prescription $\boldsymbol{\beta}^I=0$ on $\partial\mathcal{B}$ does not introduce a severe constraint on the distribution of debonding in those problems where $\boldsymbol{\beta}$ takes non-null values close to the boundary.

Box 4.BVP for the HPFRC composite.

$$\nabla\cdot\boldsymbol{\sigma}+\mathbf{b}=\mathbf{0},\quad\forall\,\mathbf{x}\in\mathfrak{B}\tag{59}$$

$$\tilde{\tau}_f^I-\frac{A_f}{\Pi_f}(\tilde{\sigma}_f^I)_{,r}=0,\quad\forall\,\mathbf{x}\in\mathfrak{B}\quad(I=1,\dots,n_f)\tag{60}$$

$$\boldsymbol{\sigma}=\hat{\boldsymbol{\sigma}}(\mathbf{u},\boldsymbol{\beta},\boldsymbol{\alpha});\quad\tilde{\sigma}_f=\hat{\tilde{\sigma}}_f(\varepsilon_f,\alpha_f);\quad\tilde{\tau}_f=\hat{\tilde{\tau}}_f(\beta,\alpha_\gamma)$$

$$\mathbf{u}=\mathbf{u}^*\quad\forall\,\mathbf{x}\in\partial\mathfrak{B}_u$$

$$\boldsymbol{\sigma}\cdot\mathbf{n}=\mathbf{t}^*\quad\forall\,\mathbf{x}\in\partial\mathfrak{B}_\sigma\tag{61}$$

$$\beta^I=0\quad\forall\,\mathbf{x}\in\partial\mathfrak{B}\quad(I=1,\dots,n_f)$$

In order to derive the variational BVP for a *HPFRC* composite, the virtual variations of the configurational space are defined as follows:

$$\begin{aligned}&\mathcal{V}_0=\{\delta_{\mathbf{u}}|\delta\mathbf{u}=\mathbf{0},\quad\forall\mathbf{x}\in\partial\mathfrak{B}_u\}\\&\mathcal{V}_0^\beta=\partial\beta^{(I)}|\partial\beta^{(I)}=0,\quad\forall\mathbf{x}\in\partial\mathfrak{B}\quad(I=1,\dots,n_f)\end{aligned}\tag{62}$$

Notice that variations of $\boldsymbol{\beta}$, one for every index $I$, are considered with fixed direction. Then, (59) and (60) are alternatively formulated using a variational approach:

$$\int_{\mathfrak{B}}(\nabla\cdot\boldsymbol{\sigma}+\mathbf{b})\cdot\delta\mathbf{u}\,dV=0,\quad\forall\delta\mathbf{u}\in\mathcal{V}_0\tag{63}$$

$$\int_{\mathfrak{B}}(\hat{\tilde{\tau}}_f^{(I)}-\frac{A_f}{\Pi_f}(\hat{\tilde{\sigma}}_f^{(I)})_{,r})\cdot\delta\beta^{(I)}\,dV=\mathbf{0},\quad\forall\delta\beta^{(I)}\in\mathcal{V}_0^\beta\quad(I=1,\dots,n_f)\tag{64}$$

The microstructure variational equation (64) comes from admitting arbitrary scalar variations, $\delta\beta^I$, which are associated with the r-component of $\boldsymbol{\beta}^I$. Integrating (63) and (64) by parts, using the Green's identity and including the boundary conditions (61), the variational BVP can be written as shown in equation (65) and (66) in Box 5. In equation (65), $\hat{\boldsymbol{\sigma}}$ is the stress evaluated through the constitutive model: $\boldsymbol{\sigma}=\hat{\boldsymbol{\sigma}}(\mathbf{u},\boldsymbol{\beta},\nabla\boldsymbol{\beta},\boldsymbol{\alpha})$. Similarly, $\hat{\tilde{\sigma}}_f^I$ and $\hat{\tilde{\tau}}_f^I$ in (66) are the average fiber stress and average bond shear stress in the interface zone evaluated through the constitutive equations of Box 2 and 3.

Box 5.Variational BVP for the HPFRC composite.

Find : $\mathbf{u}(\mathbf{x},t)$ and $\beta(\mathbf{x},t)$; $\forall\mathbf{x}\in\mathfrak{B}$ fulfilling,

$$\int_{\mathfrak{B}}\hat{\boldsymbol{\sigma}}:\nabla^s\delta\mathbf{u}\,dV-\int_{\mathfrak{B}}\mathbf{b}\cdot\delta\mathbf{u}\,dV-\int_{\Gamma_\sigma}\mathbf{t}^*\cdot\delta\mathbf{u}\,dS=0;\quad\forall\delta\mathbf{u}\in\mathcal{V}_0\tag{65}$$

$$\int_{\mathfrak{B}}\left(\hat{\tilde{\tau}}_f^I\delta\beta^{(I)}+\frac{A_f}{\Pi_f}\hat{\tilde{\sigma}}_f^{(I)}(\delta\beta^{(I)})_{,r^I}\right)dV=0;\quad\forall\delta\beta^{(I)}\in\mathcal{V}_0^\beta\quad(I=1,\dots,n_f)\tag{66}$$

## 5. Numerical implementation of the HPRFC model

This Section presents an outline of the finite element formulation and the implementation of the HPFRC model. Additional detailed descriptions of both aspects of the methodology are going to be addressed by the authors in a forthcoming paper.

### 5.1. The Finite element model

A mixed finite element with equal order interpolation for the displacement, $\mathbf{u}$, and each of the microslip, $\beta^I$ (for $I = 1, \ldots, n_f$), is here proposed. The spatial discretization reads for these cases,

$$\hat{\mathbf{u}}(\mathbf{x}, t) = \sum_{j=1}^{n_{node}} N_j(\mathbf{x}) \mathbf{q}_j(t) \tag{67}$$

$$\hat{\beta}^I(\mathbf{x}, t) = \sum_{j=1}^{n_{node}} N_j(\mathbf{x}) p_j^I(t) \tag{68}$$

where $n_{node}$ stands for the number of nodes in the finite element mesh, $N_j(\mathbf{x})$ are the standard shape functions, $\mathbf{q}_j$ and $p_j^I$ are the displacements and the $I$-th micro-slip of the node $j$-th, respectively. The corresponding spatial discretization of the variational displacement fields $\delta\mathbf{u}$ and $\delta\beta$ reads,

$$\delta\hat{\mathbf{u}}(\mathbf{x}), = \sum_{j=1}^{n_{node}} N_j(\mathbf{x}) \delta\mathbf{q}_j \tag{69}$$

$$\delta\hat{\beta}^I(\mathbf{x}) = \sum_{j=1}^{n_{node}} N_j(\mathbf{x}) \delta p_j^I \tag{70}$$

where, $\delta\mathbf{q}_j$ and $\delta p_j^I$ are the corresponding variations associated with the displacement and $i$-th slip of the $j$-th node, respectively. Substitution of the approximate solution, (67) and (68) and the variational fields (69) and (70), into the variational BVP in Box 5, yields the discrete form in Box 6. Eq. (71) is the standard finite element equilibrium discrete equation, where $\mathbf{R}$ is the vector of residual forces, $\mathbf{B}^e$ is the stain–displacement matrix, $\hat{\sigma}$ represents the stress term provided by the constitutive model: $\hat{\boldsymbol{\sigma}}(\mathbf{p}, \mathbf{q}, \boldsymbol{\alpha})$ (with $\mathbf{p} = [p^1, \ldots, p^{n_f}]$), $\Lambda$ is the element assembling operator, $n_{elem}$ is the number of finite elements in the mesh and $\mathbf{F}^{ext}$ is the vector of conventional external forces. In Eq. (72), $[\mathbf{N}]^e$ and $[\mathbf{N}]^e_{,r}$ are the nodal shape functions and their derivatives (with respect to the $r$-coordinate), respectively, arranged as a vector.

The coupled system of Eqs. (71) and (72) is solved iteratively by means of a Newton–Raphson scheme. In each iteration, the incremental solution $(\Delta\mathbf{p}, \Delta\mathbf{q})$, at time $t + \Delta t$, is found by means of a one-way coupled staggered scheme, where the variables $(\Delta\mathbf{p})_{t+\Delta t}$ are solved by freezing the variables $(\Delta\mathbf{q}^I)_t$. After that, a correction step is performed by evaluating $(\Delta\mathbf{q}^I)_{t+\Delta t}$, for $I = 1, \ldots, n_f$, and holding fixed $(\Delta\mathbf{p})_{t+\Delta t}$. This step is computationally inexpensive.

Box 6.Discrete form of the variational BVP for the HPFRC composite.

Find : $\mathbf{q}(t)$ and $p^I(\mathbf{x}, t)$ $(I = 1, 2, \ldots, n_f)$; fulfilling

$$\mathbf{R} = \bigwedge_{e=1}^{n_{elem}} \int_{\Omega^e} (\mathbf{B}^e)^T \hat{\boldsymbol{\sigma}} d\Omega^e + \mathbf{F}^{ext} = \mathbf{0} \tag{71}$$

$$\bigwedge_{e=1}^{n_{elem}} \int_{\Omega^e} \left( [\mathbf{N}]^e \hat{\tilde{\tau}}_f^{(I)} + \frac{A_f}{II_f} [\mathbf{N}]^e_{,r} \hat{\tilde{\sigma}}_f^{(I)} \right) d\Omega^e = \mathbf{0}; \quad (I = 1, \ldots, n_f) \tag{72}$$

### 5.2. The fracture model

The structural strength of HPFRC composites is highly dependent on the crack evolution across the meso and macro-structure. The non-linear response displayed by this material takes place during the cement cracking stage and the complete response depends dramatically on the very strong interaction between concrete cracks and the fiber–matrix bond slip mechanism, whose model was presented in previous sections. Thus, besides considering the bond-slip mechanisms, it is necessary to account for the concrete crack phenomena to establish a satisfactory constitutive model of the composite material.

There have been numerous approaches in the literature for modeling concrete fracture problems. Some contributions of the authors in this field, following the strong discontinuity approach, are presented in Oliver et al. (2002), Oliver and Huespe (2004) and Sánchez et al. (2012). A book, with an up to date description of different techniques and models addressed to this problems, has recently been published by Hofstetter and Meschke, 2011.

In the present formulation, we use a numerical model described in Oliver et al. (2010) and Dias et al. (2011). This methodology makes use of a localized strain injection procedure via mixed formulations that reduces the sophistication presented by alternative techniques. Details about the implementation of this fracture model in the HPFRC composite will be addressed by the authors in a forthcoming paper.

## 6. Model assessment

Different aspects of the proposed methodology are validated through several examples. In all cases, the numerical solutions are contrasted with experimental results.

The first example corresponds to a conventional bending beam test with reinforced fibers distributed in only one (horizontal) direction. In the second example, a dogbone strip under uniaxial tensile stress is simulated: first, for the plain specimen (without reinforcement fibers), and then, for the specimen having a random distribution of fibers.

### 6.1. Four-point bending beam test

It is a well known fact that the shape of the reinforcement fibers has a direct relationship with the bond-slip mechanism because it modifies substantially the pull-out force. Based on this idea, Jiang et al. (2000), have reported the experimental results of a four-point bending test using HPFRC beams build with two types of steel-wire-reinforcements: (a) conventional-straight-short fibers (CSS), and (b) bone-shaped-short fibers (BSS). With these experiments, the authors have compared the effectiveness of BSS reinforcements, with respect to the CSS ones, to improve the mechanical properties of reinforced cement. Also, in both cases, they have reported the crack pattern that was observed after the occurrence of structural failure and how the cracks have propagated across the beam.

Using the reported results in Jiang et al. (2000), we evaluate the model capacity to capture the wide range of structural responses caused by different reinforcement fiber shapes.

The four-point bending beam that was experimentally tested is shown in Fig. 5a, with the geometrical dimensions and loads. Fig. 5b depicts the sizes and shapes of the CSS and the BSS reinforcement fibers used to reinforce the beam, and Fig. 5d shows the layout of the spatial reinforcement fibers embedded into the concrete, all of them are horizontally oriented and distributed as shown in Fig. 5d. In consequence, only one bundle of fibers can represent this composite.

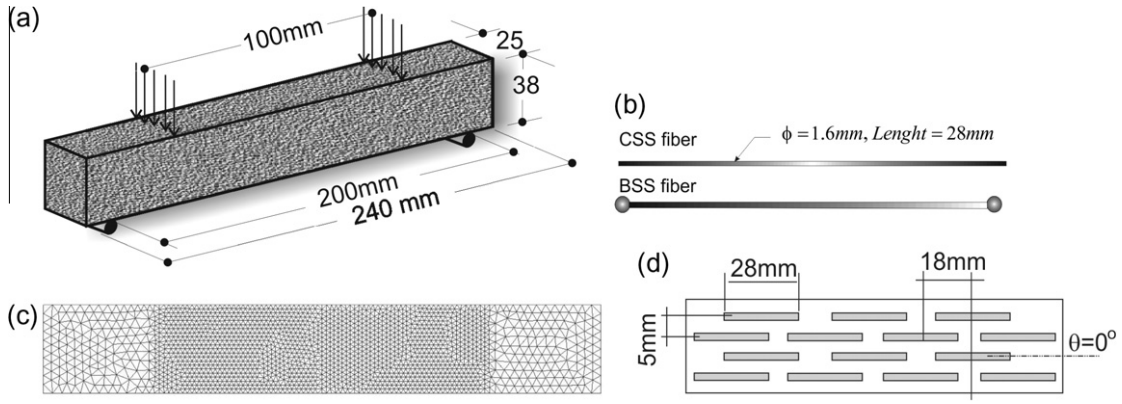


**Fig. 5.** Four-point bending beam test. (a) Beam geometry and set-up of the test; (b) schematic illustration of the BSS- and CSS-steel-wire reinforcements, both fibers have identical diameters and lengths; (c) finite element mesh and (d) distribution of the reinforcement fiber in the concrete.

**Table 1**
Four-point bending beam test. Material properties (the notation of the parameters agrees with that of Boxes 1 and 2).

| Matrix | Fiber | Interface |
|---|---|---|
| $\sigma_m^{ut} = 4.0$ MPa | $\sigma_f^y = 260$ MPa | $\tau_\Gamma^u =$ different values |
| $E_m = 21.$GPa | $E_f = 180$ GPa | $G_\Gamma = 1.e5$ GPa/m |
| $\nu_m = 0.2$ | $H_f = 700$ MPa | $H_\Gamma = 0$ MPa/m<br>$\tau_\Gamma^R = 0$ MPa |
| $G_{m_f} = 100$ N/m | $\theta = 0°$ | $k_f = 0.86\%$ |

The numerical simulation is performed by assuming a two-dimensional plane stress model. A triangular finite element mesh with 3900 elements, as shown in Fig. 5c, with three degrees of freedom per node (two for displacements and one for $\beta$), is used for the numerical simulation. The material properties are indicated in Table 1.

Fig. 6a compares the total load $P$ versus the middle point vertical displacement response. In the Figure, we compare the experimental results, of the reinforced CSS and BSS-wire-reinforced specimens, with the numerical solution obtained for the ultimate bond strength $\tau_\Gamma^u = 2.5$ MPa (conforming to a weak bond) and $\tau_\Gamma^u = 7.5$ MPa (conforming to a strong bond). It can be observed that for both values of $\tau_\Gamma^u$, the results closely reproduce the experimental observations for the CSS and BSS specimens.

According to the reference work, the first crack in the BSS specimen was observed at a load: $P = 1500$ N, while in the CSS specimen, it was: $P = 1280$ N. From these results, we observe in Fig. 6a the dramatic increase of ductility and the apparent toughness (energy consumed till the complete loss of structural load-carrying capacity) of the beam built with the BSS reinforcement fiber.

Several values of the ultimate bond stress $\tau_\Gamma^u$ were tested in order to evaluate the sensitivity of the model performance with this parameter. In Fig. 6b we compare the numerical solutions obtained with a set of parameters $\tau_\Gamma^u$, in the interval: $[2.5, 7.5]$ MPa. Notice how the model capture the increase of ductility, as far as the ultimate bond strength, $\tau_\Gamma^u$, becomes larger.

*6.1.1. Post-failure examination*

According to Jiang et al. (2000), Fig. 7a shows the experimental failure mechanism result of the CSS specimen which failed by a single crack. In contrast, Fig. 7b shows the BSS specimen after failure displaying a more distributed and multiple crack patterns.

With the present model and using several ultimate bond strengths, $\tau_\Gamma^u$ $(= 2.5, 4.5, 5.5, 7.5$ MPa) we have obtained the iso-displacement contour lines displayed in Fig. 8(a) (c) (e) and (g). In these pictures, the coalescence of a number of iso-lines represents the formation of cracks. The damage distributions in the concrete are shown in Fig. 8(b) (d) (f) and (h) by means of iso-color maps. Darker color in the damage map indicates a larger damage values, and therefore, a more degraded material. From these Figures, we can observe that, the larger the parameter $\tau_\Gamma^u$, the closer is the fracture pattern to the experimental result observed in the BSS specimen displaying multiple crack formation. Alternatively, by adopting lesser values of $\tau_\Gamma^u$, it is possible to simulate a single crack fracture mode, typical of light reinforced concrete.

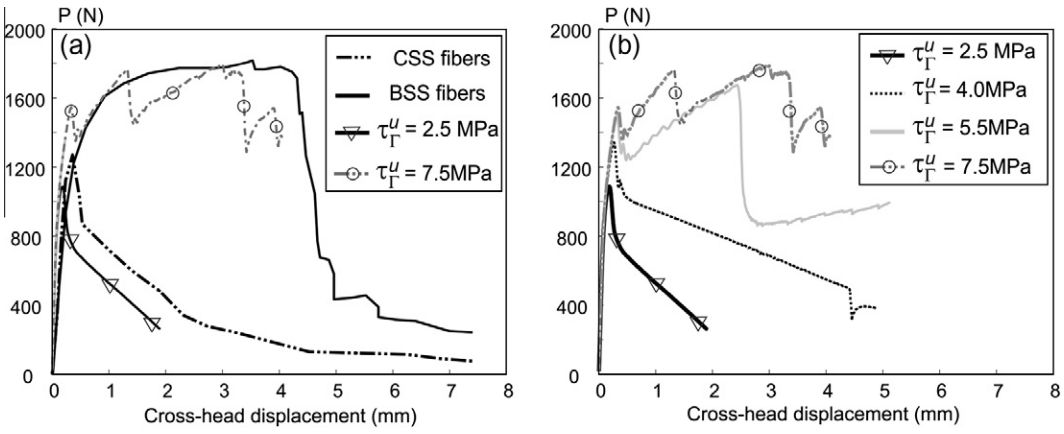


**Fig. 6.** Four-point bending beam test. Load as a function of cross head displacement steel–wire–reinforced cement specimens: (a) comparison between experiments and numerical results using the material parameter: $\tau_\Gamma^u = 2.5$ MPa and $\tau_\Gamma^u = 7.5$ MPa, respectively and (b) load vs. cross head displacement curves for different values of: $\tau_\Gamma^u$.

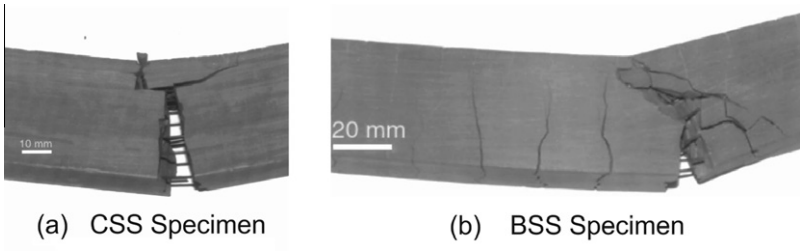


**Fig. 7.** Four-point bending beam test. Crack pattern and failure modes: (a) CSS and (b) BSS specimens reported in Jiang et al. (2000).

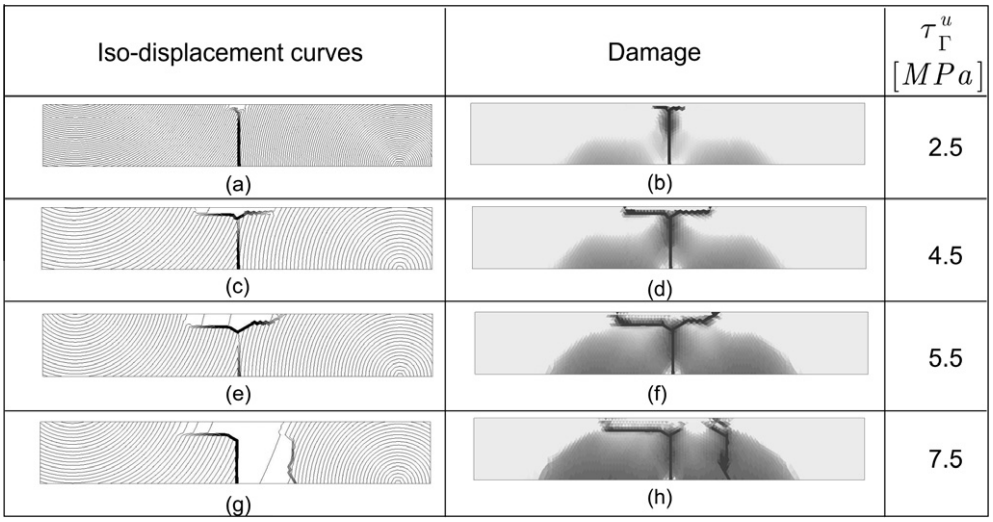


**Fig. 8.** CSS- and BSS-wire reinforced beam ($k_f = 1\%$). Numerical results: iso-displacement curves and damage level depicting the crack patterns for different values of the ultimate bond shear strength.

The single crack pattern observed for $\tau_\Gamma^u = 2.5$ MPa is also replicated for $\tau_\Gamma^u = 4.0$ MPa and $\tau_\Gamma^u = 5.5$ MPa. Experimentally, in the CSS-wire reinforced specimen (Fig. 7a), the crack branched out of the transverse plane at the end of the test. Thus, the crack patterns simulated with the ultimate bond strengths: $\tau_\Gamma^u = 4.0$ MPa and $\tau_\Gamma^u = 5.5$ MPa coincides more closely with the experimental result than that, obtained with: $\tau_\Gamma^u = 2.5$ MPa.

### 6.2. Tensile tests of a dogbone shape specimen

Fig. 9a and c illustrates a dogbone shape specimen that have been subjected to a series of experimental tests by Suwannakarn (2009). From these tests, two specific cases are here considered: (a) plain mortar without reinforcement fibers presented in Section 6.2.1, and (b) HPFRC composite with a random distribution of hooked end fibers presented in Section 6.2.2.

In both cases, the numerical simulation uses a two-dimensional plane stress model that is depicted in Fig. 10a. The finite element mesh is shown in Fig. 10b. In the experimental setup, the average elongation was obtained by measuring the relative displacement between points E and F (Fig. 10a) that are spaced about 178 mm.

#### 6.2.1. Tensile test of a mortar specimen without reinforcement

Under monotonic tensile loading, the specimen without reinforcing fibers, failed in a brittle manner. Only a single crack was observed. Results of experimental tests show that the average stress–strain behavior of mortar specimens does not exhibit perfect linear behavior. Moreover, the measured Young's modulus, $E_m$, ranged between [7804—26717] MPa with an average value: $E_m = 13886$ MPa, significantly less than the Young's modulus for standard concretes. Suwannakarn pointed out that this low stiffness results from the lack of coarse aggregates in the mortar composition of the specimens. The ultimate tensile strength of mortar, $\sigma_m^{ut}$, shows also a large dispersion. The average value was estimated to be: $\sigma_m^{ut} = 1.25$ MPa. Suwannakarn acknowledges that the large dispersion of both parameters, $E_m$ and $\sigma_m^{ut}$, is due to the characteristic sensitivity of brittle materials, like mortar, to the gripping conditions, and the variation due to mortar mixing and curing.

Fig. 11a shows the average stress–average strain curve obtained with the numerical simulations. It is compared with the scattered results that were presented in the reference experimental work. As can be observed in Fig. 11a, the softening branch has not been reported in the experimental results. Then, as a rough estimation of the mortar fracture energy, we adopt: $G_{m_f} = 100$ N/m, which is a similar value to that generally considered for standard concrete.

A failure mode displaying a single crack is observed in the experimental results (Fig. 11b, left). A similar failure mechanism is observed at the end of the numerical analysis (Fig. 11b, right), where the vertical iso-displacement lines make evident this result. In order to trigger the strain localization process in the specimen center, we perturb the model by defining a weaker single finite element in the middle of the specimen (in where $\sigma_m^{ut}$ is reduced 10% of the bulk value).

#### 6.2.2. Tensile test of the HPFRC composite

An identical specimen such as that depicted in Fig. 9, is analyzed in this section. The material is a HPFRC composite with high strength steel fibers, and with hooked end (commercially known under the trademark "Dramix®"). The fiber diameter and length is: 0.4 mm and 30 mm, respectively. In the reference work, Suwan-

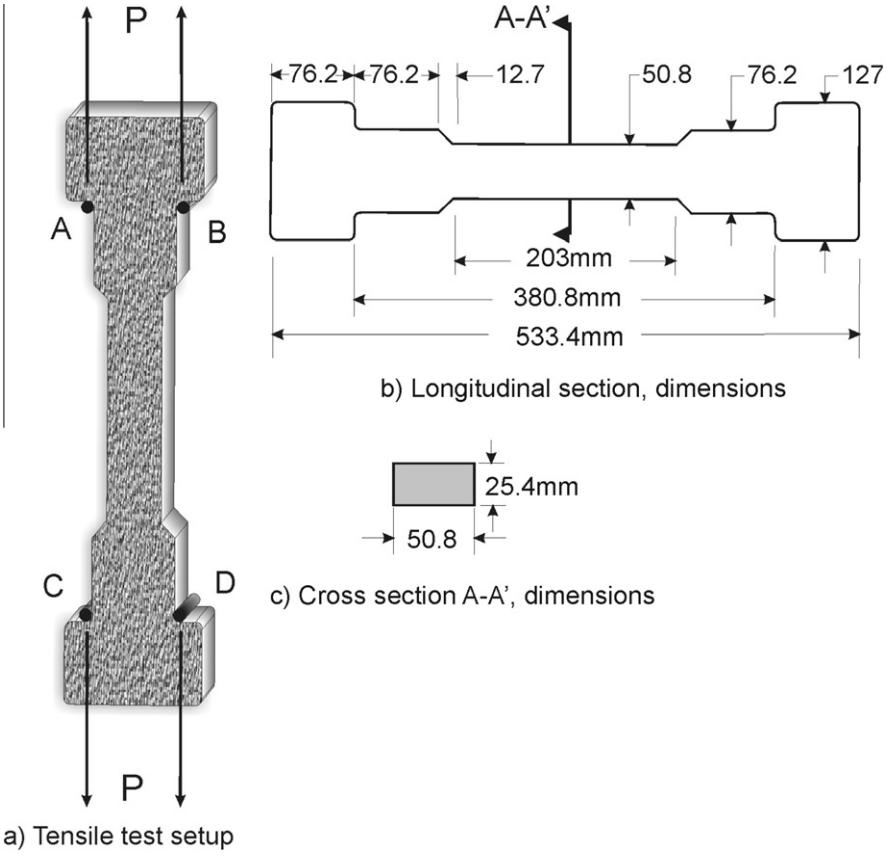


**Fig. 9.** Tensile test of a dogbone shape specimen (Suwannakarn, 2009).

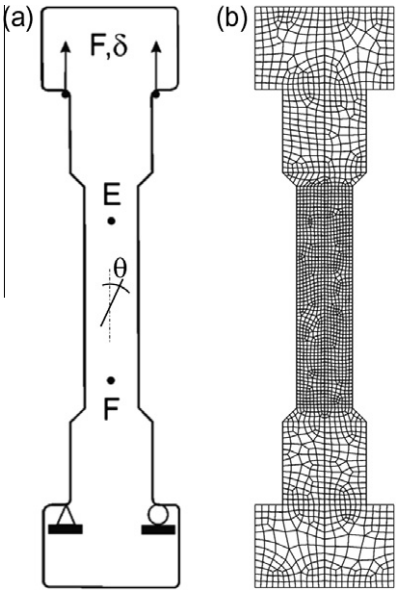


**Fig. 10.** Tensile test of a dogbone shape specimen. (a) Numerical test layout. (b) Finite element mesh with 1967 quadrilateral elements.

nakarn mentions that the composite material has been manufactured through mixing of the components, including fibers, and its posterior pouring into moulds to obtain the specimens. However, he does not specify clearly how the fibers are distributed in the specimen during its preparation. Considering this observation, and even noting that fibers are larger than the thickness of the specimen, we assume that fibers have a uniform distribution in all directions (in the three-dimensional space).

We model this problem as a two-dimensional plane stress case. Then, the contribution of the out-of-plane fibers to the plane of analysis are projected, using an orientation factor, following a technique described in the literature (see Dupont and Vandewalle, 2005). We simulate the reinforcement distribution by adopting nine fiber bundles directed along the angles described in Table 2. The angle: $\theta = 0^\circ$ coincides with the principal (average) stretch direction (see Fig. 10a).

In Table 2, the mechanical properties of the matrix are drawn from the tensile test of the specimen without fibers that is numerically reported in the previous section. The fiber parameters, as well as the interface parameters: $\sigma_f^y$, $E_f$, $\tau_\Gamma^u$ and $k_f$ are taken from the reference work, while the fiber and interface hardening moduli: $H_f$, $H_\Gamma$ have been estimated from numerical adjustments. The elastic modulus $G_\Gamma$ is defined with an arbitrarily large value, such that an almost rigid-plastic model is recovered for describing the fiber–matrix bond response, as also, a null bond residual stress ($\tau_\Gamma^R = 0$ MPa) is assumed in this model.

The average stress vs. average strain experimental results are described through the lower and upper envelopes depicted in Fig. 12. The numerical solution is superimposed in the same figure. A rough, but acceptable, description of the specimen response is observed.

The numerical result shows a well defined point indicating the first crack in the matrix, which is identified, in Fig. 12, with the point where the stress–strain linear response is lost (point A). Furthermore, comparing with the unreinforced case of Fig. 11a (note the different orders of magnitude in the scale of strains), the HPFRC composite response shows a notable hardening after the initiation of the first crack. In the last case, a notable strain hardening effect

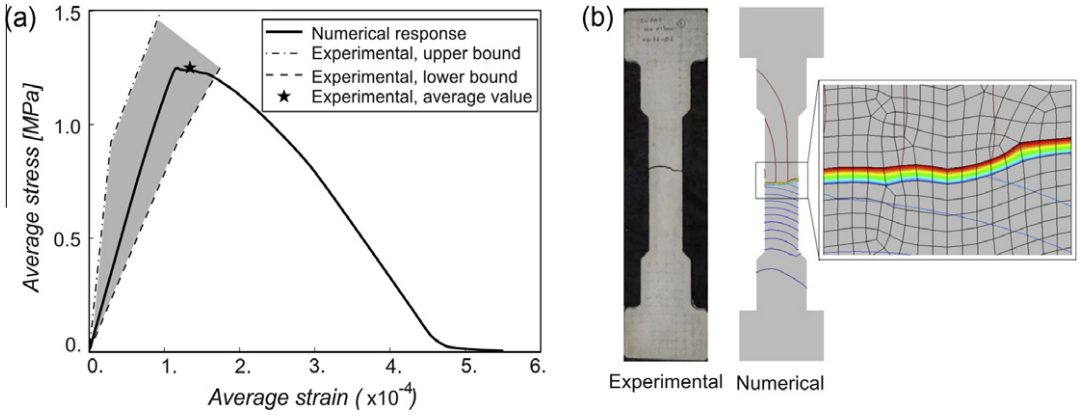


**Fig. 11.** Tensile test of the dogbone shape specimen, mortar without fibers. (a) Average stress vs. average strain (measured through the relative displacement between points E–F); (b) iso-displacement lines at the end of analysis displaying the formation of a single crack, compared with the experimental result (specimen 3, p. 59 in Suwannakarn (2009)).

**Table 2**
Material properties of the generic HPFRC composite specimen (notation of parameters agrees with that of Boxes 1 and 2).

| Matrix | Fiber | Interface |
|---|---|---|
| $\sigma_m^{ut} = 1.25$ MPa | $\sigma_f^y = 2100$ MPa | $\tau_\Gamma^u = 5.1$ MPa |
| $E_m = 13.9$ GPa | $E_f = 210.$GPa | $G_\Gamma = 1.e5$ GPa/m |
| $\nu_m = 0.2$ | $H_f = 100$ MPa | $H_\Gamma = 100$ MPa/m<br>$\tau_\Gamma^R = 0$ *MPa* |
| $G_{m_f} = 100$ N/m | $\theta = \begin{bmatrix} 0°, 10°, 20°, 30°, 45°, \\ 60°, 70°, 80°, 90° \end{bmatrix}$ | $k_f = 0.75\%$ |

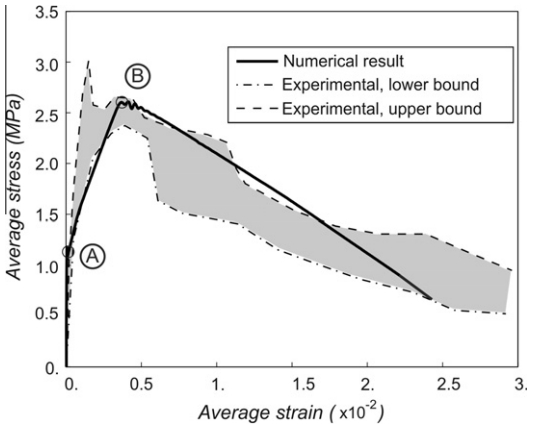


**Fig. 12.** HPFRC dogbone shape specimen subjected to the tensile test. Comparison between experimental and numerical results. Experimental test correspond to the High Strength Hooked Steel fibers case (specimen D-H-H-0.75, p. 80 in Suwannakarn (2009)).

occurs after the first crack initiation till the strain value of 0.004 (point B) is reached. This strain value corresponds with the peak load, and it agrees reasonably well with the experimental data. Also, we note that the post-peak behavior is not very well captured by the model. While the experiments shows a post-peak response with a long tail (a usual characteristic in HPRFC specimens), the almost straight post-peak behavior, predicted by the numerical solution, may be due to the null value that we have adopted for the residual bond strength parameter: $\tau_\Gamma^R$.

*6.2.2.1. Bridging effect induced by the reinforcement fibers.* Pictures in Fig. 13 depict iso-damage color maps, and illustrate different stages during the evolution of the matrix damage distribution. The numbers below every picture identify the loading stages where the corresponding damage distribution is taken. These stage numbers agree with the points marked in Fig. 15, which plots the average stress–strain curve. As expected, high values of matrix damage are observed in early stages (Stage 2). In Stages 3 and 4, before the strain localization onset, large areas of the specimen are severely damaged. Nevertheless, no noticeable reduction of the structural load carrying capacity is detected.

In Stages 5 and 7, the strain localization process is almost completed. In the localization band, the value of the damage indicates that the matrix is almost exhausted. However, the stress–strain curve, at Stage 7, shows a residual, not null, structural load carrying capacity.

The results above mentioned, before and after crossing the structural limit point, evidence an appropriate capturing of the fiber bridging effect during the matrix cracking process taking place in the specimen.

*6.2.2.2. Analysis of the fiber–matrix debonding effect.* During the stretching process, debonding and pullout of the fibers is expected. Pullout phenomena involve complex failure processes. And it is even more complex when the fibers are not parallel to the pullout direction. For example, the so called snubbing friction (Li et al., 1990) which is due to the intense shearing at the point where the fiber exits the matrix. This effect produces an increased resistance of the pullout force displayed by inclined flexible fibers. On the contrary, pullout resistance of inclined fibers can be decreased by spalling of the matrix, especially for stiff fibers. These complex effects are not included in the present model. Even though, as it will be shown in this Section, the gross macroscopic description of HPFRC composite specimens with random distribution of fibers can be acceptably captured by the present model.

Let us analyze three bundles of fibers (at 0°, 45° and 90° with respect to the loading direction.

Fig. 14 depicts several entries of picture pairs. Every picture pair represents the results corresponding to a given fiber bundle, oriented in the direction specified in the left column of the figure, and at different loading stages during the stretching process. The stage numbers displayed below the pictures agree with the points marked in Fig. 15. In the left column of every picture pair, the finite elements reaching the ultimate bond strengths, $\tau_\Gamma^u$, are colored. In the right column of every pair, the finite elements reaching the fiber yield stress, $\sigma_f^y$, are colored.

As shown in Fig. 14, Stages number (3) and (4) stay on the hardening regime. During this regime, some fibers reach the ultimate bond strengths while they remain in elastic regime. Experimental

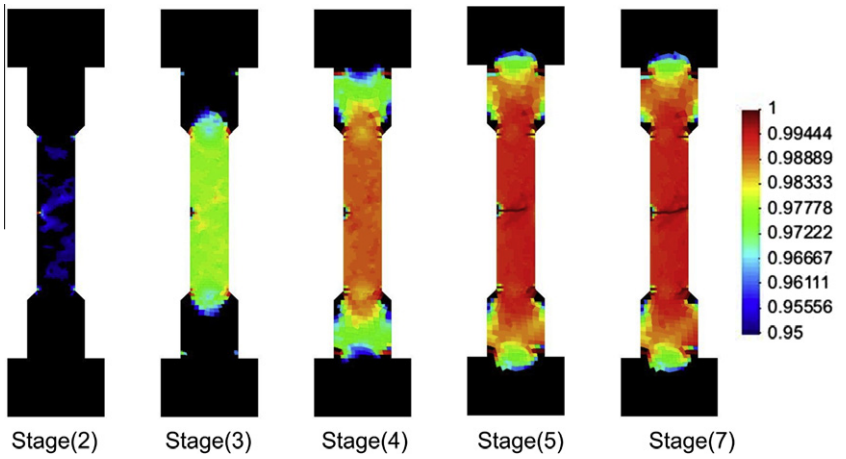


**Fig. 13.** HPFRC dogbone shape specimen subjected to the tensile test. Different stages of damage evolution.

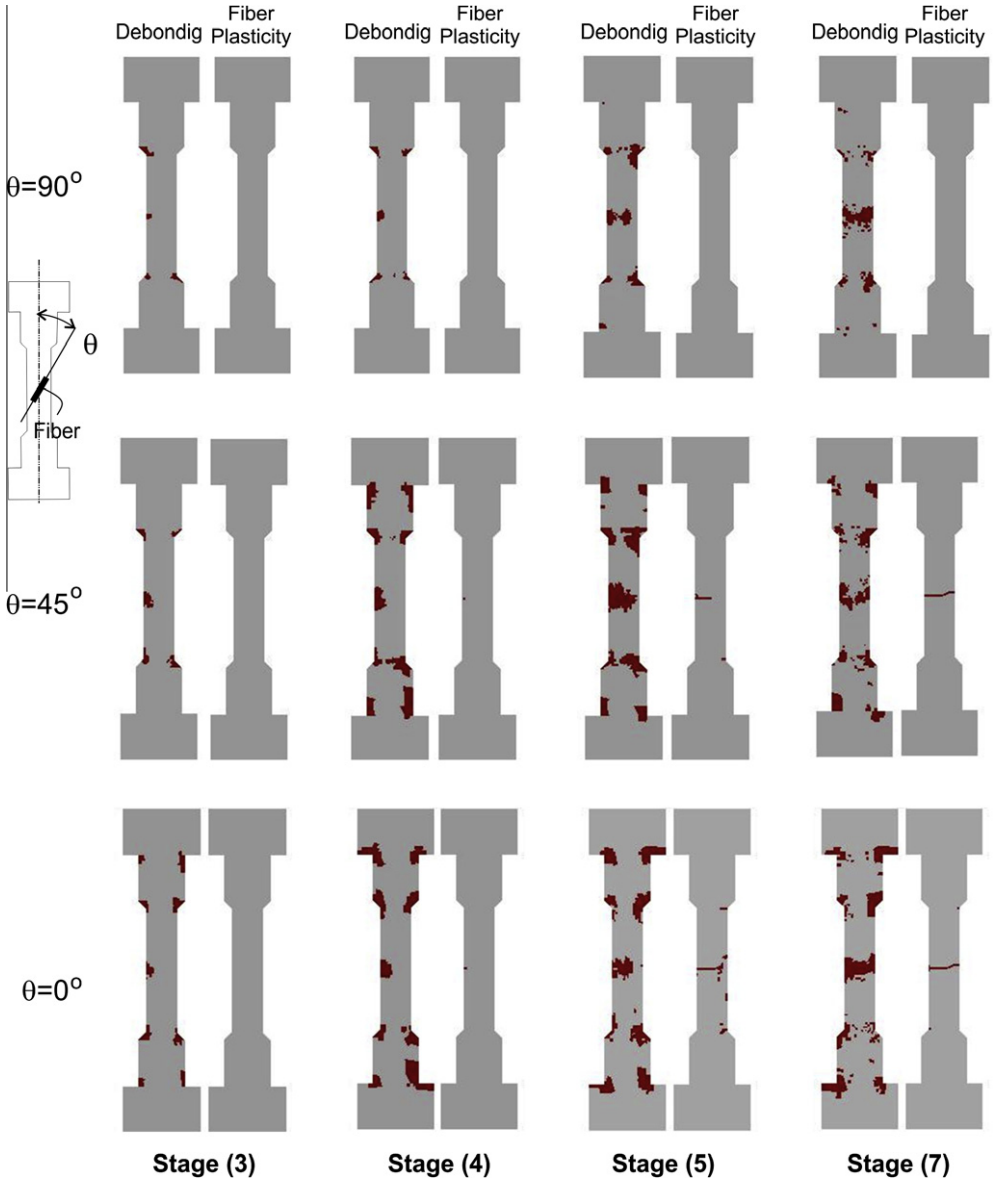


**Fig. 14.** HPFRC dogbone shape specimen subjected to the tensile test. Analysis of the debonding mechanism for different fiber bundles: $\theta = 0°, 45°, 90°$. Left column for every entry (debonding): elements reaching the ultimate bond shear stress: $\tau_f^u$. Right column for every entry (fiber plasticity): elements reaching the fiber yield stress $\sigma_f^y$.

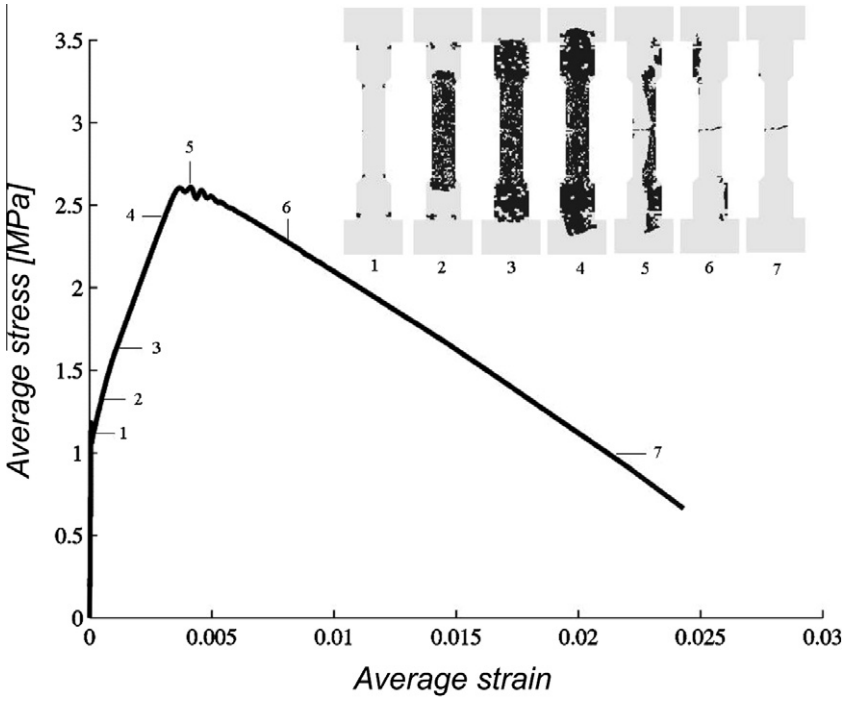


**Fig. 15.** HPFRC dogbone shape specimen tensile test. Average stress vs. average strain numerical curve. Insert: in black it is represented the finite elements with injected enhanced strains to capture the strong discontinuity solution (see additional details in Oliver et al., 2010; Dias et al., 2011).

works (Laranjeira et al., 2010a,b) indicate that inclined fibers, with small angles with respect to the load direction, show improved pullout performances. According with this observation, we see that in Stage (3) and for the aligned fibers ($\theta = 0^\circ$), more elements achieve the ultimate bond strength than for the inclined ones ($\theta = 90^\circ$). Debonding mechanisms evolve significantly for aligned fibers in the Stage (4), while not so much for the horizontal ones.

Stages (5) and (7) stay on the structural postcritical regime. The matrix is severely damaged and the strain localization process has initiated in the center of the specimen, as also, near the transition zones, where changes the width of the sample. Then, a very complex stress–strain distribution in the specimen center is calculated. During these stages, the horizontal fibers remain elastic ($\theta = 90^\circ$), while the inclined and aligned ones ($\theta = 45^\circ$, $\theta = 0^\circ$), reach the yield condition in those finite elements that are intersected by the crack path. Additionally, in the strain localization zones, we note that matrix–fiber debonding is observed for all fibers, whatever their directions are. Then, we conclude that the complex process of straining, in the localization zones, produce the fiber–matrix debonding effect, even for fibers orthogonal to the principal crack path. We cannot confirm at the present, if this result is only a numerical model response or it has a physical significance.

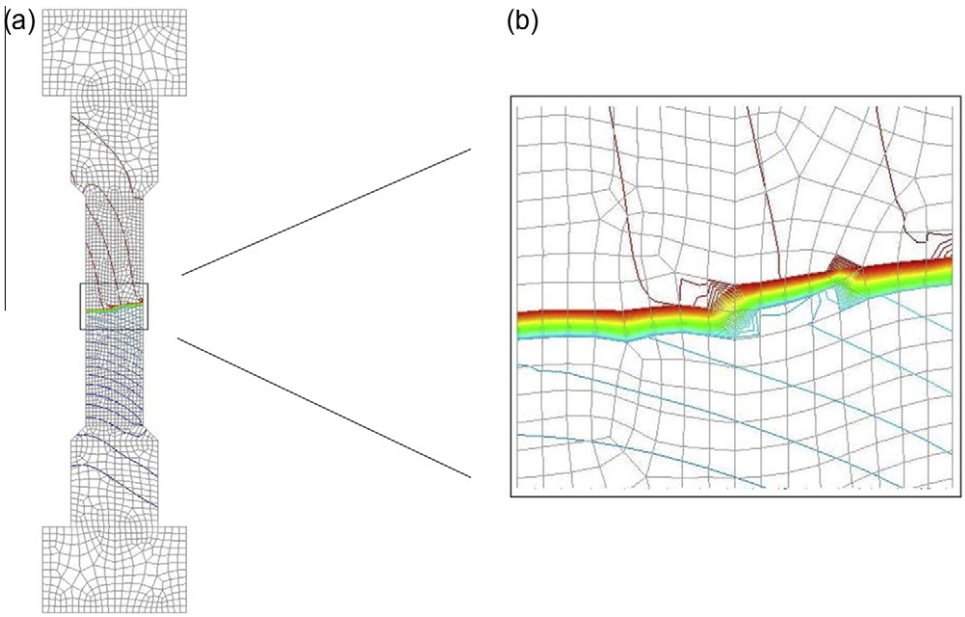


**Fig. 16.** Tensile test of the dogbone shape specimen. HPFRC composite with hooked end fibers. Iso-displacement contour lines at the end of the analysis.

*6.2.2.3. Strain localization phenomenon.* Fig. 15 illustrates the average stress–average strain numerical curve. The pictures inserted in Fig. 15 corresponding to Stages 1–7, depict the evolution of the domain where elements with enhanced strain modes are injected. These strain modes are injected once the matrix reaches a critical condition and have the objective of capturing the strong discontinuity solution (see additional details about this technique in Oliver et al., 2010; Dias et al., 2011).

The results displayed in the insert of Fig. 15 suggest that the critical matrix condition initiates at the beginning of the hardening process, Stage (1). Then, during Stage (4), the injection domain extends through most of the specimen. However, during the Stage (5), the number of injected elements (those which remain in the critical condition) reduces dramatically, and at the end of the simulation process, only the elements on the failure path stay in this condition.

Fig. 16 plots the vertical iso-displacement lines at the end of analysis. This picture represents the strain localization pattern provided by the numerical solution. Only one single macrocrack is observed in the specimen. Unfortunately, direct comparison with experimental results is not possible because no crack pattern (for this specific test) is reported in the work of Suwannakarn.

From this analysis, we can conclude that the model captures very well the process of multiple cracking (Stages 2–4) and the subsequent fracture localization (Stages 5–7) which are typical of the HPFRC composites in general (see, e.g. Naaman, 2007a,b).

## 7. Conclusions

In this paper, a novel formulation for HPFRC composites based on the notion of micromorphic materials is presented. The formulation uses a morphological kinematic descriptor that characterizes a key mesostructural phenomenon: the fiber–matrix bond slip mechanism. The mechanical interactions, taking place in the composite, due to this phenomenon are manifested once the conjugated terms of the morphological descriptor: i.e. the generalized micro-stresses and micro-forces, are introduced in the model and the mechanical power is defined. The general framework of the Multifield Theory then specifies the balance equations that govern these generalized micro-stresses and micro-forces.

As a consequence of these very basic suppositions in the mechanical model, new degrees of freedoms (in the continuum) are incorporated into the theoretical formulation of the model, one for every considered morphological descriptor. An important conceptual notion is that these d.o.f.'s are independent of those defining the spatial placement of the body. In this HPFRC model, there is one morphological descriptor for every fiber bundle (orientation) considered.

The material model description is completed once the free energy of the composite, jointly with its functional dependence on the kinematical variables and their gradients, is defined. In the present model, we adopt the mixture theory to define the composite free energy. Then, the overall free energy is the addition of every component free energy, (including as such, the power expended by the cohesive mechanism in the fiber–matrix bond) times the volume fraction of the component.

The finite element technique, as also the fracture model, used in the numerical implementation has only been sketched in the paper. These important aspects of the numerical methodology will be fully described by the authors in a forthcoming paper. Even when these aspects have not been detailed, we have presented two numerical examples that illustrate the most relevant properties of the model:

i. The first example demonstrates the model capability to represent adequately the effects having a key mesoscopic phenomenon on the overall macroscopic response of HPFRC composite structures. Specifically the toughness sensitivity with the fiber-matrix bond strength, during the fracture process of specimens.
ii. In the second examples, more specific mesostructural effects induced by the same mechanism were deeply analyzed. For example, the sensitivity of the model for capturing different amount of fiber plastic deformation and debonding with the orientation of the fiber bundles.

Finally, we should mention that the fractional step (staggered) algorithm implemented to solve the discrete problem, including the additional d.o.f.'s associated with the micromorphic fields, preserves the computational cost in the same order shown by standard finite element formulations in displacements.

## Acknowledgments

The Spanish Ministry of Science and Innovation, and the Catalan Government Research Department, are gratefully acknowledged for financial support under Grants BIA2011-24258 and 2009 SGR 1510, respectively. The third author acknowledges the financial support from CONICET (PIP 2010-2012).

We want to express our gratitude to the Reviewers of this paper because their suggestions have helped us to notably improve the manuscript.

## Appendix I. Symmetry of the stress tensor

We show that the angular momentum balance equation arising in the HPFRC model, when it is derived from the multifield theory (Mariano, 2002; Mariano and Stazi, 2005; Capriz and Mariano, 2001), results in the classical angular momentum balance equation of the conventional continuum mechanics specifying the symmetry of the stress tensor $\boldsymbol{\sigma}$.

First, we derive the transformation law of $\dot{\boldsymbol{\beta}}$ under an observer change. Let us consider the expression (8), (24) and (26):

$$\boldsymbol{\beta} = \beta(r,s,t)\mathbf{r}; \quad \mathbf{S} = \sigma_{rr}(r,s,t)(\mathbf{r}\otimes\mathbf{r}); \quad \mathbf{z} = z_r\mathbf{r} \tag{AI.1}$$

where $z_R$ is the r-component of $\mathbf{z}$. Also, consider that $\boldsymbol{\beta}$ is the micromorphic field described by the observer 1 and $\hat{\boldsymbol{\beta}}$ is the same entity described by the observer 2. Both observers differing by a time dependent rotation: $\mathbf{Q}(t)$, where $\mathbf{Q}\in SO(3)$ is a time dependent second order rotation tensor, plus a time dependent translation. Then, given the rate of the micromorphic field $\dot{\boldsymbol{\beta}}$ described by the observer 1, the same entity described by the observer 2, and denoted $\dot{\hat{\boldsymbol{\beta}}}$, is:

$$\dot{\hat{\boldsymbol{\beta}}}|_{\mathbf{Q}=1} = \overline{(\beta\dot{\mathbf{Q}}\mathbf{r})}|_{\mathbf{Q}=1} = [\dot{\boldsymbol{\beta}}\mathbf{Q}\mathbf{r} + \beta\dot{\mathbf{Q}}\mathbf{r} + \beta\mathbf{Q}\dot{\mathbf{r}}]|_{\mathbf{Q}=1} = \dot{\boldsymbol{\beta}} + \mathbf{Q}\dot{\mathbf{Q}}|_{\mathbf{Q}=1}\boldsymbol{\beta} \tag{AI.2}$$

In these expressions, the axial vector, spin, of the instantaneous rotation velocity, of one observer respect to the other: $(\mathbf{Q}\dot{\mathbf{Q}}|_{\mathbf{Q}=1})$, is denoted with $\mathbf{q}$ and the following identity follows: $\mathbf{Q}\dot{\mathbf{Q}}|_{\mathbf{Q}=1}\boldsymbol{\beta} = \mathbf{q}\wedge\boldsymbol{\beta}$. Introducing the third order permutation tensor $\mathbf{e}$ ($\mathbf{e}_{ijk}=1$ if $(i,j,k)$ is an even permutation of $(1,2,3)$, $\mathbf{e}_{ijk}=-1$ if it is an odd permutation, and 0 if any index is repeated), such that: $\mathbf{q}\wedge\boldsymbol{\beta} = \mathbf{e}:(\mathbf{q}\otimes\beta)$, in (AI.2) we can write: $\mathbf{Q}\dot{\mathbf{Q}}|_{\mathbf{Q}=1}\beta = (-\mathbf{e}\boldsymbol{\beta})\mathbf{q} = \mathcal{A}\mathbf{q}$, where the operator:

$$\mathcal{A} = \frac{d\dot{\boldsymbol{\beta}}}{d\mathbf{q}} = -\mathbf{e}\boldsymbol{\beta} \tag{AI.3}$$

Due to the co-linearity of $\boldsymbol{\beta}$ and $\mathbf{z}$, it results, for any arbitrary rotation $\mathbf{Q}$, that:

$$\mathcal{A}^T\mathbf{z} = \mathbf{0} \tag{AI.4}$$

and expressing $(\nabla\mathcal{A}^T)\mathbf{S}$ in indicial notation, it also results in:

$$(\nabla \mathcal{A}^T)\mathbf{s} = -e_{ijk}\frac{\partial \beta_k}{\partial x_l}s_{jl} = \mathbf{0} \tag{AI.5}$$

because the indices ($j$, $l$ and $k$) are identical. With (AI.4) and (AI.5), we conclude that the angular momentum balance equation (Eq. (18) in Mariano and Stazi (2005)):

$$skew(\boldsymbol{\sigma}) = \mathcal{A}^T\mathbf{z} + (\nabla \mathcal{A}^T)\mathbf{s} = \mathbf{0} \tag{AI.6}$$

turns out to be the classical angular momentum balance equation of the conventional continuum mechanics, form where the symmetry of the conventional stress tensor must be enforced.

## References


Bolander, J.E., Sukumar, N., 2005. Irregular lattice model for quasistatic crack propagation. Phys. Rev. B 71, 094106.

Bolander, J., Choi, S., Duddukuri, S., 2008. Fracture of fiber-reinforced cement composites: effects of fiber dispersion. Int. J. Fract. 154, 73–86.

Boulfiza, M., 1998. Constitutive modeling of Fiber Reinfoced Cement Composites. Ph.D. Department of Civil Engineering. The University of British Columbie Vancouver.

Capriz, G., 1989. Continua with Microstructure. Springer Verlag, Berlin.

Capriz, G., Mariano, P.M., 2001. Multifield theories: an introduction. Int. J. Solids Struct. 38 (6–7), 939–941.

Car, E., Zalamea, F., Oller, S., Miquel, J., Oñate, E., 2002. Numerical simulation of fiber reinforced composite materials-two procedures. Int. J. Solids Struct. 39, 1967–1986.

Dias, I.F., Oliver, J., Huespe, A.E., 2011. Strain injection, mixed formulations and strong discontinuities in fracture modeling of quasi-brittle materials. In: Congress on Numerical Methods in Engineering, APMTAC, Coimbra, Portugal.

Dupont, D., Vandewalle, L., 2005. Distribution of steel fibres in rectangular sections. Cement Concr. Compos. 27, 391–398.

Eringen, A.C., Suhubi, E.S., 1964. Nonlinear theory of simple micro-elastic solids—I. Int. J. Eng. Sci. 2, 189–203.

Ferrara Liberato, R.G., 2000, Non-local damage analysis of three-point on SFRC notched beams. In: Fiber Reinforced concrete (FRC) BEFIB' 2000.

Ferreira, L., 2007. Fracture analysis of a high-strength concrete and a high-strength steel–fiber–reinforced concrete. Mech. Compos. Mater. 43, 479–486.

Forest, S., 2009. Micromorphic approach for gradient elasticity, viscoplasticity, and damage. J. Eng. Mech. 135, 117–131.

Frémond, M., Nedjar, B., 1996. Damage, gradient of damage and principle of virtual power. Int. J. Solids Struct. 33, 1083–1103.

Guerrero, P., Naaman, A.E., 2000. Effect of mortar fineness and adhesive agents on the pull-out response of steel fibers. ACI Mater. J. 97, 12–20.

Hirschberger, C.B., Sukumar, N., Steinmann, P., 2008. Computational homogenization of material layers with micromorphic mesostructure. Philos. Mag. 88, 3603–3631.

Hofstetter, G., Meschke, G., 2011. Numerical Modeling of Concrete Cracking. Springer.

Jiang, H., Valdez, J.A., Zhu, Y.T., Beyerlein, I.J., Lowe, T.C., 2000. The strength and toughness of cement reinforced with bone-shaped steel wires. Compos. Sci. Technol. 60, 1753–1761.

Kabele, P., 2007. Multiscale framework for modeling of fracture in high performance fiber reinforced cementitious composites. Eng. Fract. Mech. 74, 194–209.

Kim, D.P., Naaman, A.E., El-Tawil, S., 2009. High performance fiber ReforcJed cement composites with innovative sliphardening twisted steel fibers. Int. J. Concr. Struct. Mater. 3, 119–126.

Laranjeira, F., Aguado, A., Molins, C., 2010a. Predicting the pullout response of inclined straight steel fibers. Mater. Struct. 43, 875–895.

Laranjeira, F., Molins, C., Aguado, A., 2010b. Predicting the pullout response of inclined hooked steel fibers. Cement Concr. Res. 40, 1471–1487.

Linero, D.L., 2006. A Model of Material Failure for Reinforced Concrete via Continuum Strong Discontinuity Approach and Mixing Theory. PhD. Thesis, Politech. Univ. Catalunya, Barcelona, Spain.

Linero, D., Oliver, J., Huespe, A.E., 2010. Simulación numérica del proceso de fractura en concreto reforzado mediante la metodología de discontinuidades fuertes de continuo. Parte I: formulación. Rev. Ing. Investig. (Ing. Investig.). 30(2), 5–15.

Li, V.C., Wang, Y., Backer, S., 1990. Effect of inclining angle, bundling and surface treatment on synthetic fibre pull-out from a cement matrix. Composites 21 (2), 132–140.

Li, V.C., Stang, H., 1997. Interface property characterization and strengthening mechanisms in fiber reinforced cement based composites. Adv. Cement Based Mater. 6, 1–20.

Li, F., Li, Z., 2000. Continuum damage mechanics based modeling of fiber reinforced concrete in tension. Int. J. Solids Struct. 38, 777–793.

Marco, M., 2006. Uniqueness and minimum theorems for a multifield model of brittle solids. Int. J. Solids Struct. 43, 3428–3443.

Mariano, P.M., 2002. Multifield theories in mechanics of solids. Adv. Appl. Mech. 38, 1–93.

Mariano, P., Stazi, F., 2005. Computational aspects of the mechanics of complex materials. Arch. Comput. Methods Eng. 12, 391–478.

Mindlin, R.D., 1964. Micro-structure in linear elasticity. Arch. Ration. Mech. Anal. 16, 51–78.

Naaman, A.E., Namur, G.J., Alwan, J., Najm, H., 1991a. Fiber pull-out and bond slip. Part I: Analytical study. ASCE J. Struct. Eng. 117, 2769–2790.

Naaman, A.E., Namur, G.J., Alwan, J., Najm, H., 1991b. Fiber pull-out and bond slip. Part II: Experimental validation. ASCE J. Struct. Eng. 117, 2791–2800.

Naaman, A.E., 2003. Engineered steel fibers with optimal properties for reinforcement of cement composites. J. Adv. Concr. Technol. 1, 241–252.

Naaman, A.E., 2007a. Tensile strain-hardening FRC composites: historical evolution since the 1960. In: Grosse, C.U. (Ed.), Advances in Construction Materials 2007. Springer, Berlin, Heidelberg, pp. 181–202.

Naaman, A.E., 2007b. High performance fiber reinforced cement composites. In: Caijun, , Mo, Y.L. (Eds.), High Performance Construction Materials – Science and Applications. World Scientific Publishing Co. Pte. Ltd., pp. 91–153 (Chapter 3).

Oliver, J., Huespe, A.E., Pulido, M.D., Samaniego, E., Chavez, E., 2002. From continuum mechanics to fracture mechanics: the strong discontinuity approach. Eng. Fract. Mech. 69 (2), 113–136.

Oliver, J., Huespe, A.E., 2004. Theoretical and computational issues in modelling material failure in strong discontinuity scenarios. Comput. Methods Appl. Mech. Eng. 193, 2987–3014.

Oliver, J., Dias, I.F., Huespe, A.E., 2010, Strong discontinuities, mixed finite element formulations and strain localization in fracture modeling of quasi-brittle materials. In: Bicanic et al. (Eds.) EURO-C 2010, March 15–18, 2010, Rohrmoos, Austria. Computational Modelling of Concrete Structures. Taylor & Francis Group, London. ISBN 978-0-415-58479-1.

Oliver, J., Linero, D.L., Huespe, A.E., Manzoli, O.L., 2008. Two-dimensional modeling of material failure in reinforced concrete by means of a continuum strong discontinuity approach. Comput. Methods Appl. Mech. Eng. 197, 332–348.

Oller, S., Oñate, E., Miquel, J., Botello, S., 1996. A plastic damage constitutive model for composite materials. Int. J. Solids Struct. 33, 2501–2518.

Peng, X., Meyer, C., 2000. A continuum damage mechanics model for concrete reinforced with randomly distributed short fibers. Comput. Struct. 78, 505–515.

Pros, A., Diez, P., Molins, C., 2012. Modeling steel fiber reinforced concrete: numerical immersed boundary approach and a phenomenological mesomodel for concrete–fiber interaction. Int. J. Numer. Methods Eng. 90, 65–86.

Sánchez, P.J., Huespe, A.E., Oliver, J., Sonzogni, V., 2012. A macroscopic damage-plastic constitutive law for modeling quasi-brittle fracture and ductile behaviour of concrete. Int. J. Numer. Anal. Methods Geomech. 36, 546–573.

Shannag, M., Hnasen, W., Tjiptobroto, P., 1999. Interface debonding in fiber reinfoorced cement–matrix composites. J. Compos. Mater. 33, 158–176.

Sirijaroonchai, K., El-Tawil, S., Parra-Montesinos, G., 2010. Behavior of high performance fiber reinforced cement composites under multi-axial compressive loading. Cement Concr. Compos. 32, 62–72.

Suwannakarn, S.W., 2009. Post-Cracking Characteristics of High Performance Fiber Reinforced Cementitious Composites. University of Michigan.

Trusdell, C., Toupin, R., 1960. The Classical Field Theory. Springer-Verlag, Berlin.

Zhang, J., Li, V.C., Nowak, A.S., Wang, S., 2002. Introducing ductile strip for durability enhancement of concrete slabs. J. Mater. Civil Eng. 14, 253–261.